Structural and Multidisciplinary Optimization (2026) 69:12
https://doi.org/10.1007/s00158-025-04216-3

RESEARCH PAPER

Topology optimization on variable curved surfaces for mass and heat transfer in surface flow

Yongbo Deng[1] · **Jan G. Korvink**[1]

Received: 16 June 2025 / Revised: 5 November 2025 / Accepted: 23 November 2025 / Published online: 22 December 2025

Abstract

This paper develops a mathematical framework that extends topology optimization for mass and heat transfer onto variable 2-manifolds, which are curved surfaces defined as the design domains allowed to evolve rather than remain fixed during the optimization process. Consequently, the design freedom of topology optimization is increased by incorporating the design domains themselves into the design space. The variable curved surfaces expressed as the implicit 2-manifolds are homeomorphously defined on predetermined fixed base manifolds. The concept of fiber bundle is used to describe the pattern of a surface structure together with the implicit 2-manifold as an integrated ensemble defined on the base manifold. Therefore, this topology optimization on variable 2-manifolds is developed to optimize the matching between the patterns of surface structures and the implicit 2-manifolds defined with the patterns. It is implemented based on the porous medium model by using the material distribution method, where the material density is used to interpolate the impermeability of the porous medium filled on the implicit 2-manifolds. Two sets of design variables are defined for the patterns of the surface structures and the implicit 2-manifolds, respectively. They are regularized by two surface-PDE filters and a parameter is introduced to the surface-PDE filter of the implicit 2-manifolds to control the variable magnitude. The topology optimization problems are analyzed by using the continuous adjoint method to derive the gradient information of the design objectives and constraints. They are then solved by using the gradient based iterative procedures numerically implemented based on the surface finite element method. To permit the use of linear surface elements for the consideration of computational cost, the variational formulations of the surface Navier–Stokes equations, surface convection-diffusion equation and surface convective heat-transfer equation are stabilized by using the Brezzi-Pitkäranta, Petrov-Galerkin and general least square techniques, respectively. The adjoint equations are derived for the stabilized variational formulations of those governing equations. In the numerical results, the variable amplitude in the surface-PDE filter of the implicit 2-manifolds, Reynolds number, Péclet number, pressure drop and dissipation power of the surface flow are investigated to demonstrate the increased design freedom and extended design space achieved by topology optimization on variable 2-manifolds for mass and heat transfer in surface flow.

Keywords Topology optimization · 2-manifold · Fiber bundle · Surface flow · Material distribution method · Mass and heat transfer

1 Introduction

Topology optimization is a robust computational method for determining the optimal structural configuration, corresponding to the material distribution within a structure (Bendsøe and Sigmund 2003). Unlike size and shape optimization, which relies on adjusting a limited number of geometric parameters, topology optimization explores the full design space to generate structures that meet user-defined performance objectives. Because it is less dependent on the initial design guess, topology optimization offers greater flexibility and robustness. Consequently, it serves as a more

Responsible Editor: Qing Li.

✉ Yongbo Deng
yongbo.deng@kit.edu

Jan G. Korvink
jan.korvink@kit.edu

[1] Institute of Microstructure Technology (IMT), Karlsruhe Institute of Technology (KIT), Hermann-von-Helmholtzplatz 1, 76344 Eggenstein-Leopoldshafen, Germany

powerful tool for optimizing structures where the material distribution is represented by design variables.

Optimization of structural topology was investigated as early as 1904 for truss structures (Michell 1904). Topology optimization originated from structural optimization problems in elasticity and compliant mechanisms (Bendsøe and Kikuchi 1988; Cheng and Olhoff 1981; Sigmund 2001, 1997; Saxena 2005). It was later extended to a variety of physical domains, including acoustics, electromagnetics, fluidics, optics, thermodynamics, etc. (Borrvall and Petersson 2003; Gersborg-Hansen et al. 2006; Nomura et al. 2007; Sigmund and Hougaard 2008; Duhring et al. 2008; Akl et al. 2008; Xue et al. 2024). Over the years, numerous approaches have been developed to implement topology optimization, such as evolutionary techniques (Steven et al. 2000), the evolutionary structural optimization (ESO) method (Huang and Xie 2010; Nabaki et al. 2018), the homogenization method (Bendsøe and Kikuchi 1988; Allaire 2002), the material distribution or variable density method (Rozvany 2001; Bendsøye and Sigmund 1999), the level set method (Wang et al. 2003; Allaire et al. 2004; Liu and Korvink 2008; Xing et al. 2010; Xia and Wang 2008), the method of moving morphable components (MMC) (Guo et al. 2014, 2016), the feature-driven method (Zhou et al. 2016), and the phase-field method (Takezawa et al. 2010). As one of the most widely used approaches in topology optimization, the material distribution method performs the optimization by assigning a density variable that represents the amount of material present at each point within the design domain. This method offers advantages such as rapid convergence, low sensitivity to the initial design guess, and the capability to handle multiple constraints. Therefore, it is adopted to carry out the research presented in this paper.

Topology optimization for fluid problems was first pioneered using evolutionary techniques (Steven et al. 2000). The first application of the material distribution-based topology optimization to Stokes flow was reported in 2003 (Borrvall and Petersson 2003). This approach was further investigated for Stokes flow (Guillaume and Idris 2004; Aage et al. 2008) and Darcy-Stokes flow (Guest and Proevost 2006; Wiker et al. 2007), where an artificial friction force proportional to the fluid velocity was introduced into the Stokes equations to enable topology optimization based on the porous medium model proposed in Ref. (Borrvall and Petersson 2003). The optimization framework was subsequently extended to Navier–Stokes flow at low and moderate Reynolds numbers (Gersborg-Hansen et al. 2005; Olessen et al. 2006; Deng et al. 2010), as well as to non-Newtonian flow (Pingen and Maute 2010). Early studies on topology optimization for fluid problems primarily focused on steady flow without body forces (Bendsøe and Sigmund 2003; Borrvall and Petersson 2003; Gersborg-Hansen et al. 2005; Olessen et al. 2006; Aage et al. 2008; Guest and Proevost 2006; Deng et al. 2010; Wiker et al. 2007; Zhou and Li 2008; Pingen and Maute 2010; Challis and Guest 2009). However, unsteady flow are ubiquitous in practical applications. To address this, topology optimization was extended to unsteady Navier-Stokes flow to capture the influence of flow dynamics on the optimal topology (Kreissl et al. 2011; Deng et al. 2011). In many fluid systems, external body forces associated with fluid inertia, such as gravity, centrifugal and Coriolis forces, are also significant. Topology optimization of steady and unsteady Navier–Stokes flow with body forces has been achieved by penalizing the body force through an interpolation function of the design variable and by employing the level set method, respectively (Deng et al. 2013a, b). High-velocity fluid transport often leads to turbulence, which is common in industrial applications. Topology optimization for turbulent flow at high Reynolds numbers has been developed based on the finite-volume discretized Reynolds-averaged Navier–Stokes (RANS) equations, coupled with either one- or two-equation turbulence closure models (Dilgen et al. 2018), the Spalart-Allmaras model (Yoon 2016; Sá et al. 2021), or data-driven models (Hammond et al. 2022). Building on these developments, topology optimization has been successfully applied to the design of microfluidic devices, including micromixers (Andreasen et al. 2009; Deng et al. 2012), microvalves (Deng et al. 2010; Liu et al. 2012), and micropumps (Deng et al. 2011).

Topology optimization for surface flow has been developed to determine the optimal patterns of corresponding surface structures (Deng et al. 2022, 2024). Modeling fluid motion as surface flow can significantly reduce the computational cost in the numerical design of fluidic structures. For example, the flow within channels attached to the walls of equipment can be represented as surface flow on curved surfaces corresponding to the outer geometries of the equipment. Likewise, the streamsurfaces associated with the outer shapes of fluidic structures under complete-slip boundary conditions can be regarded as surface flow decoupled from the volume flow. Such complete-slip boundaries can be approximated or realized by several methods, including chemically coating or physically structuring solid surfaces to induce extreme hydrophobicity (Kown et al. 2009), applying optimal control techniques to manipulate boundary velocities (Sritharan 1998), or generating vapor layers between the solid and liquid phases through the Leidenfrost effect (Thimbleby 1989). To achieve topology optimization of surface structure patterns, research has been conducted on stiffness and multi-material structures (Vermaak et al. 2014; Sigmund and Torquato 1997; Gao and Zhang 2011; Luo et al. 2012; Wang and Wang 2004; Zhou and Wang 2007; Vogiatzis et al. 2018), shell structure layouts(Krog and Olhoff 1996; Ansola et al. 2002; Hassani et al. 2013; Lochner-Aldinger and Schumacher 2014; Clausen et al. 2017; Dienemann et al. 2017; Yan et al. 2018), electrode patterns for electroosmosis (Deng et al. 2018), fluid–structure and fluid–particle interactions (Yoon 2010;

Lundgaard et al. 2018; Andreasen 2019), energy absorption (Andreasen 2012), cohesion (Behrou et al. 2017), actuation (Raulli and Maute 2005), and wettability control (Deng et al. 2018, 2019, 2020), among other topics. Topology optimization on 2-manifolds has been developed for applications in elasticity, wettability control, heat transfer, and electromagnetics, where a 2-manifold refers to a smooth curved surface that is a topological space locally homeomorphic to a Euclidean plane (Huo et al. 2022; Zhang and Feng 2022; Deng et al. 2020); and topology optimization on variable 2-manifolds has been developed for wettability control at fluid/solid interfaces (Deng et al. 2020). Recently, topology optimization for surface flow has extended the design space of fluidic structures to 2-manifolds (Deng et al. 2022). Topology optimization for surface flow on variable 2-manifolds has been developed to match the patterns of the surface flow and the implicit 2-manifolds defined with the patterns (Deng et al. 2024). The design space and design freedom for flow problems were subsequently expanded by incorporating the design domains associated with surface flow patterns into the design space. These design domains correspond to implicit 2-manifolds that are defined on predetermined fixed 2-manifolds represented as geometrical surfaces.

Mass and heat transfer are two fundamental and ubiquitous phenomena in fluid flow. Due to scaling effects, microflow typically operates in the laminar regime, where convection is weak and diffusion dominates the mass and heat transfer processes. This often results in relatively low transfer efficiency. Consequently, enhancing mass and heat transfer efficiency in microflow has become a long-standing and critical topic in the development of microfluidic devices for industrial applications (Nguyen and Wu 2005; Yao et al. 2015; Miralles et al. 2013). Topology optimization has emerged as one of the most effective approaches to enhance mass and heat transfer in microflow by optimizing microfluidic structures to strengthen convective transport (Høghøj 2023; Tawk et al. 2019; Marck et al. 2013). In the context of mass transfer, topology optimization has been applied to the design of micromixers and microreactors (Andreasen et al. 2009; Deng et al. 2012; Okkels and Bruus 2006; Schäpper et al. 2011; Wang et al. 2023; Bhattacharjee and Atta 2022; Chen et al. 2021). For heat transfer, it has been implemented in the optimization of heat sinks and heat exchangers (Fawaz et al. 2022; Zhang and Liu 2008; Rogié and Andreasen 2023; Pietropaoli et al. 2019; Alexandersen et al. 2013; Lohan et al. 2017; Li et al. 2018; Zhang and Gao 2019; Joo et al. 2017; Yan et al. 2023; Høghøj et al. 2020; Li et al. 2019; Xia et al. 2023). Most of these studies have been conducted either in three-dimensional (3D) domains or on simplified two-dimensional (2D) planes. With the manufacturability enabled by modern additive manufacturing and 3D-printing technologies, topology optimization on 2-manifolds offers new design opportunities for mass and heat transfer problems. Furthermore, topology optimization on variable 2-manifolds can enhance the design freedom by optimizing the matching between surface structure patterns and the implicit 2-manifolds on which they are defined. Therefore, this paper develops a topology optimization framework on variable 2-manifolds for mass and heat transfer in surface flow.

In this paper, the surface Navier–Stokes equations, surface convection-diffusion equation and surface convective heat-transfer equation are formulated on the design domain of the pattern of the surface flow, where the design domain is a 2-manifold. This design domain is implicitly defined on a predetermined fixed 2-manifold. Two design variables are introduced, one for the design domain of the pattern and the other for the pattern of the surface flow, and they are coupled and optimized simultaneously to achieve the optimized matching between the pattern of the surface flow and its design domain. Consequently, the design domain, expressed as a 2-manifold, is implicit and variable throughout the optimization process, and is therefore referred to as a variable implicit 2-manifold.

The concept of a fiber bundle originates from differential geometry (Chern et al. 1999). A fiber bundle consists of a base manifold and a fiber that is defined over the base manifold. The pattern of the surface structure, together with its definition domain, can be regarded as the fiber of a fiber bundle. If there exists a 2-manifold that is homeomorphic to the fiber, it can be designated as the base manifold of the fiber bundle. In numerical computation, the base manifold can be predefined as a fixed geometrical surface, upon which the fiber is determined. This implies that the definition domain of the pattern is an implicit 2-manifold defined on the predefined base manifold. In this paper, the pattern of the surface flow is defined on a variable implicit 2-manifold, which serves as the design domain of the pattern. This design domain, in the form of a variable implicit 2-manifold, is itself defined on a predetermined fixed 2-manifold. The optimization of the surface flow pattern is therefore coupled with that of the variable implicit 2-manifold. The optimized matching between the pattern of the surface flow and the variable implicit 2-manifold on the predetermined fixed 2-manifold can be interpreted as the fiber of a fiber bundle. In this context, the fixed 2-manifold represents the base manifold. The description using the concept of fiber bundle highlights the integrity of the surface structure composed of implicitly defined design domain and pattern of the surface flow. It is convenient to treat the fixed 2-manifold, the variable implicit 2-manifold and the pattern of the surface flow as an integrated ensemble. Therefore, this paper adopts the concept of a fiber bundle to describe the topology of the surface structure as an integrated ensemble rather than as three separate components. Topology optimization of variable 2-manifolds for mass and heat transfer in surface flow is thus formulated as the task of finding the optimized

matching between the patterns of the surface structures and the implicit 2-manifolds defined on the prescribed base manifold, in order to achieve the desired mass and heat transfer performance (Figure 1).

The material distribution method is employed to determine the pattern of the surface structure, where the implicit 2-manifold defined with the surface structure is described on the base manifold. For the material distribution method, the porous medium model has been developed in topology optimization for fluid flow (Borrvall and Petersson 2003; Gersborg-Hansen et al. 2006; Kreissl et al. 2011; Deng et al. 2011). In the material distribution method, the porous medium model has been widely adopted in topology optimization for fluid flow (Borrvall and Petersson 2003; Gersborg-Hansen et al. 2006; Kreissl et al. 2011; Deng et al. 2011). In this model, the 2D/3D design domain is filled with a porous medium, and an artificial Darcy friction term is incorporated into the force terms of the Stokes and Navier–Stokes equations. During the optimization process, the impermeability of the porous medium evolves to yield the desired fluidic structures. Inspired by this approach, topology optimization for surface flow has been extended to 2-manifolds by filling them with a porous medium, where the artificial Darcy friction term is added to the surface Navier–Stokes equations (Deng et al. 2022, 2024). Building on this foundation, the present study applies the porous medium model to perform topology optimization on variable 2-manifolds for mass and heat transfer in surface flow.

The remained sections of this paper are organized as follows. Section 2 presents the methodology for topology optimization on variable 2-manifolds for mass and heat transfer in surface flow, including the formulation of the physical model and design variables, problem definition, adjoint analysis, and numerical implementation. Section 3 provides numerical results and discussions to demonstrate the effectiveness of the proposed topology optimization approach. Sections 4 and 5 present the conclusions and declarations, respectively. Additional material is provided in the supplementary appendix, where sections and equations are numbered with the prefix "S." Throughout this paper, the incompressible Newtonian fluid is considered. All mathematical formulations are expressed in Cartesian coordinates. Vectors are represented in column form by default, and the gradient of a vector function is defined such that the gradients of its components appear as column vectors.

2 Methodology

In this section, topology optimization on variable 2-manifolds is described for mass and heat transfer in surface flow to find the optimized matching between the patterns of the surface structures and the implicit 2-manifolds defined the surface structures. An implicit 2-manifold is homeomorphically defined on a preset base manifold. The mass and heat transfer processes are described by the surface Navier–Stokes equations, the surface convection-diffusion equation and the surface convective heat-transfer equation defined on the implicit 2-manifold.

2.1 Material interpolation

The porous medium model is utilized in topology optimization on variable 2-manifolds for mass and heat transfer in surface flow. In this model, the porous medium is filled onto the implicit 2-manifold. The artificial Darcy friction is added to the surface Navier-Stokes equations used to describe the surface flow. The artificial Darcy friction, derived based on the constitutive law of the porous medium, is assumed to be proportional to the fluid velocity (Borrvall and Petersson 2003; Gersborg-Hansen et al. 2006):

$$\mathbf{b}_\Gamma = -\alpha \mathbf{u}, \ \forall \mathbf{x}_\Gamma \in \Gamma \tag{1}$$

where $\mathbf{b}_\Gamma$ is the artificial Darcy friction force; α is the impermeability; $\mathbf{u}$ is the fluid velocity; Γ is the implicit 2-manifold; and $\mathbf{x}_\Gamma$ denotes a point on Γ. When the porosity is zero, the porous medium corresponds to a solid material with infinite impermeability and zero fluid velocity caused by the infinite friction force; when the porosity is infinite, it corresponds to the structural void for the transport of the fluid with zero impermeability. Therefore, the impermeability can be described as

$$\begin{cases} \alpha|_{\mathbf{x}_\Gamma \in \Gamma_D} = \begin{cases} +\infty, \ \gamma_p = 0 \\ 0, \ \gamma_p = 1 \end{cases} \\ \alpha|_{\mathbf{x}_\Gamma \in \Gamma_F} = 0, \ \gamma_p = 1 \end{cases} \tag{2}$$

where $\gamma_p \in \{0, 1\}$ is a binary distribution defined on Γ, with 0 and 1 representing the solid and fluid phases, respectively; Γ_D is the design domain for the pattern of the surface flow and Γ_F is the fluid domain with the material density enforced to be $\gamma_p = 1$, with Γ_D and Γ_F satisfying $\Gamma_D \cup \Gamma_F = \Gamma$ and $\Gamma_D \cap \Gamma_F = \emptyset$. Especially, Γ is the design domain, when there is no enforced fluid domain, i.e. $\Gamma_F = \emptyset$ and $\Gamma = \Gamma_D$. Equivalently, the design domain can also be specified by using an indicator defined as

$$f_{id,\Gamma}(\mathbf{x}_\Gamma) = \begin{cases} 1, \ \forall \mathbf{x}_\Gamma \in \Gamma_D \\ 0, \ \forall \mathbf{x}_\Gamma \in \Gamma \setminus \Gamma_D \end{cases} \tag{3}$$

where $f_{id,\Gamma}$ is the indicator function.

To avoid the numerical challenges on solving a binary optimization problem, the binary variable defined on the design domain is relaxed to vary continuously in [0, 1]. The relaxed

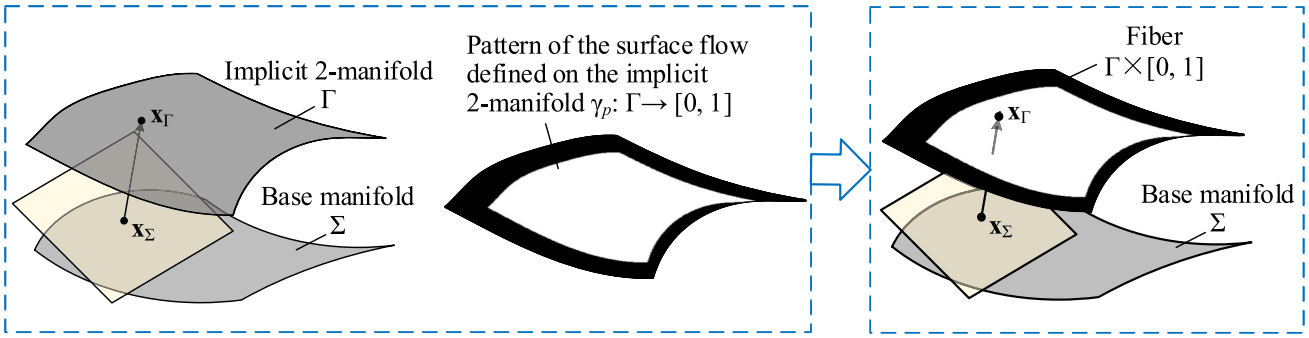

Fig. 1 Sketch for topology optimization on a variable 2-manifold for mass and heat transfer in surface flow, where the task is to find the optimized matching between the pattern of the surface structure and the implicit 2-manifold defined on the preset and fixed base manifold. Here, Γ is the implicit 2-manifold defined by a bijection on the base manifold Σ; $\mathbf{x}_\Sigma$ is a point on Σ and $\mathbf{x}_\Gamma$ on Γ is the image of $\mathbf{x}_\Sigma$; and γ_p is the pattern of the surface flow defined on the implicit 2-manifold. The implicit 2-manifold and the pattern of the surface flow together with the based manifold used to define the implicit 2-manifold compose the fiber bundle, where the fiber is spanned by the implicit 2-manifold and the pattern of the surface flow

binary variable is referred to as the design variable of the surface structure and it is used to derive the material density for the material interpolation of the impermeability. Based on the description of the impermeability in Eq. 2, the material interpolation of the impermeability can be implemented by using the convex and q-parameterized scheme (Borrvall and Petersson 2003):

$$\alpha\left(\gamma_p\right) = \begin{cases} \alpha_f + \left(\alpha_s - \alpha_f\right) q \dfrac{1-\gamma_p}{q+\gamma_p}, \ \forall \mathbf{x}_\Gamma \in \Gamma_D \\ 0, \ \forall \mathbf{x}_\Gamma \in \Gamma \setminus \Gamma_D \end{cases} \tag{4}$$

where γ_p is renamed as the material density; α_s and α_f are the impermeability of the solid and fluid phases, respectively; and q is the parameter used to tune the convexity of this interpolation. For the fluid phase, the impermeability is zero, i.e. $\alpha_f = 0$. For the solid phase, α_s should be infinite theoretically; numerically, a finite value much larger than the fluid density ρ is chosen for α_s, to simultaneously ensure the stability of the numerical implementation and approximate the solid phase with acceptable accuracy.

2.2 Design variables

In the presented topology optimization, two sets of design variables are required to be sequentially defined for the implicit 2-manifold and the pattern of the surface flow.

2.2.1 Design variable for implicit 2-manifold

To describe the implicit 2-manifold, the design variable that takes continuous values in [0, 1] is defined on the base manifold. This design variable is used to describe the distribution of the relative displacement between the implicit 2-manifold and the base manifold. The relative displacement is in the normal direction of the base manifold and the implicit 2-manifold is defined based on this normal displacement.

To ensure the smoothness of the implicit 2-manifold and the well-posedness of the solution, a surface-PDE filter is imposed on the design variable of the implicit 2-manifold (Deng et al. 2020):

$$\begin{cases} -\operatorname{div}_\Sigma\left(r_m^2 \nabla_\Sigma d_f\right) + d_f = A_d\left(d_m - \dfrac{1}{2}\right), \ \forall \mathbf{x}_\Sigma \in \Sigma \\ \mathbf{n}_{\boldsymbol{\tau}_\Sigma} \cdot \nabla_\Sigma d_f = 0, \ \forall \mathbf{x}_\Sigma \in \partial\Sigma \end{cases} \tag{5}$$

where $d_m = d_m\left(\mathbf{x}_\Sigma\right)$ is the design variable of the implicit 2-manifold; $d_f = d_f\left(\mathbf{x}_\Sigma\right)$ is the filtered design variable and it is the normal displacement used to describe the implicit 2-manifold; r_m is the filter radius, and it is constant; Σ is the base manifold used to define the implicit 2-manifold, and d_m and d_f are defined on Σ; $\mathbf{x}_\Sigma$ denotes a point on Σ; ∇_Σ and $\operatorname{div}_\Sigma$ are the tangential gradient operator and tangential divergence operator defined on Σ, respectively; $\mathbf{n}_{\boldsymbol{\tau}_\Sigma} = \mathbf{n}_\Sigma \times \boldsymbol{\tau}_\Sigma$ sketched in Fig. 2 is the unit outer conormal vector normal to $\partial\Sigma$ and tangent to Σ at $\partial\Sigma$, with $\mathbf{n}_\Sigma$ and $\boldsymbol{\tau}_\Sigma$ representing the unit normal vector on Σ and the unit tangential vector at $\partial\Sigma$, respectively; A_d is the variable amplitude of the implicit 2-manifold, i.e. the parameter used to control the variation amplitude of the normal displacement, and it is nonnegative ($A_d \geq 0$). Because d_m is valued in [0, 1], d_f is valued in $[-A_d/2, A_d/2]$. The design variable of the implicit 2-manifold and its filtered counterpart are sketched in Fig. 3.

By introducing the parameter of the variable magnitude into the surface-PDE filter in Eq. 5, the design variable of the implicit 2-manifold can be scaled onto [0, 1] which is the same as the range of the design variable of the pattern of the surface flow. The adjoint sensitivity of the design objec-

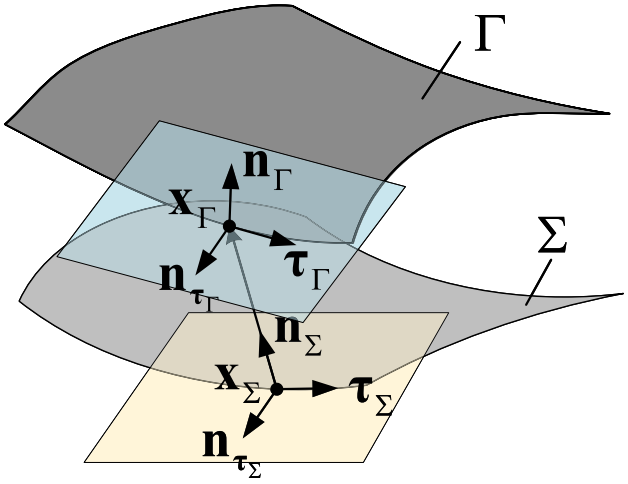

Fig. 2 Sketch for relations among the unit tangential vectors $\boldsymbol{\tau}_\Gamma$ at $\partial\Gamma$ and $\boldsymbol{\tau}_\Sigma$ at $\partial\Sigma$, the unit normal vectors $\mathbf{n}_\Gamma$ on Γ and $\mathbf{n}_\Sigma$ on Σ, the unit conormal vectors $\mathbf{n}_{\boldsymbol{\tau}_\Gamma}$ at $\partial\Gamma$ and $\mathbf{n}_{\boldsymbol{\tau}_\Sigma}$ at $\partial\Sigma$, and the tangential gradient $\nabla_\Sigma d_f$

tive to the design variable of the implicit 2-manifold can then be scaled. Simultaneously, the surface-PDE filter in Eq. 5 can ensure the smoothness of the implicit 2-manifold by reasonably choosing the filter radius. Because the surface Navier–Stokes equations, surface convection-diffusion equation and surface convective heat-transfer equation are defined on the implicit 2-manifold, the stability for the numerical solution of those surface-PDEs can be ensured.

After the filter operation, the implicit 2-manifold can be described by the filtered design variable:

$$\Gamma = \left\{ \mathbf{x}_\Gamma \,\middle|\, \mathbf{x}_\Gamma = d_f \mathbf{n}_\Sigma + \mathbf{x}_\Sigma,\ \forall \mathbf{x}_\Sigma \in \Sigma \right\} \tag{6}$$

where Γ is the implicit 2-manifold and $\mathbf{x}_\Gamma$ denotes a point on Γ. A similar relation is held for the design domain of the pattern of the surface flow, i.e.

$$\Gamma_D = \left\{ \mathbf{x}_\Gamma \,\middle|\, \mathbf{x}_\Gamma = d_f \mathbf{n}_\Sigma + \mathbf{x}_\Sigma,\ \forall \mathbf{x}_\Sigma \in \Sigma_D \right\} \tag{7}$$

where $\Sigma_D \subset \Sigma$ is the base manifold of Γ_D. From Eq. 6, a differentiable homeomorphism can be determined corresponding to the bijection $d_f : \Sigma \to \Gamma$ with $\mathbf{x}_\Gamma = d_f \mathbf{n}_\Sigma + \mathbf{x}_\Sigma$ at $\forall \mathbf{x}_\Sigma \in \Sigma$. Therefore, $\mathcal{H}(\Gamma)$ is homeomorphous to $\mathcal{H}(\Sigma)$. The Jacobian matrix of the homeomorphism in Eq. 6 for the implicit 2-manifold in the curvilinear coordinate system of the base manifold can be transformed into

$$\mathbb{T}_\Gamma = \frac{\partial \mathbf{x}_\Gamma}{\partial \mathbf{x}_\Sigma} = \nabla_\Sigma d_f \mathbf{n}_\Sigma^{\mathrm{T}} + d_f \nabla_\Sigma \mathbf{n}_\Sigma + \mathbb{I},\ \forall \mathbf{x}_\Sigma \in \Sigma \tag{8}$$

with $|\mathbb{T}_\Gamma|$ representing its determinant, where $\mathbb{I}$ is the unit tensor.

2.2.2 Design variable for pattern of surface flow

The pattern of the surface flow is represented by the material density defined on the implicit 2-manifold. The material density in Eqs. 2 and 4 is obtained by sequentially implementing the surface-PDE filter and the threshold projection on the design variable defined on the implicit 2-manifold, as sketched in Fig. 4. This design variable is also valued continuously in [0, 1]. Here, the combination of the surface-PDE filter and the threshold projection can remove the gray regions and control the minimum length scale in the derived pattern.

The surface-PDE filter for the design variable of the pattern is implemented by solving the following surface PDE (Deng et al. 2020):

$$\begin{cases} -\mathrm{div}_\Gamma \left(r_f^2 \nabla_\Gamma \gamma_f \right) + \gamma_f = \gamma,\ \forall \mathbf{x}_\Gamma \in \Gamma_D \\ \mathbf{n}_{\boldsymbol{\tau}_\Gamma} \cdot \nabla_\Gamma \gamma_f = 0,\ \forall \mathbf{x}_\Gamma \in \partial\Gamma_D \end{cases} \tag{9}$$

where γ is the design variable; γ_f is the filtered design variable; r_f is the filter radius, and it is constant; ∇_Γ and div_Γ are the tangential gradient operator and tangential divergence operator defined on the implicit 2-manifold Γ, respectively; $\mathbf{n}_{\boldsymbol{\tau}_\Gamma} = \mathbf{n}_\Gamma \times \boldsymbol{\tau}_\Gamma$ sketched in Fig. 2 is the unit outer conormal vector normal to $\partial\Gamma$ and tangent to Γ at $\partial\Gamma$, with $\mathbf{n}_\Gamma$ and $\boldsymbol{\tau}_\Gamma$ representing the unit normal vector on Γ and the unit tangential vector at $\partial\Gamma$, respectively. The threshold projection of the filtered design variable is implemented as (Wang et al. 2011; Guest et al. 2004)

$$\gamma_p = \frac{\tanh(\beta\xi) + \tanh\left(\beta\left(\gamma_f - \xi\right)\right)}{\tanh(\beta\xi) + \tanh\left(\beta\left(1 - \xi\right)\right)},\ \forall \mathbf{x}_\Gamma \in \Gamma_D \tag{10}$$

where β and ξ are the parameters of the threshold projection, with values chosen based on numerical experiments (Guest et al. 2004).

2.2.3 Coupling of design variables

The design variable introduced in Section 2.2.2 for the pattern of the surface flow is defined on the implicit 2-manifold introduced in Section 2.2.1. Their coupling relation can be derived by transforming the tangential gradient operator ∇_Γ, the tangential divergence operator div_Γ and the unit normal $\mathbf{n}_\Gamma$ into the forms defined on the base manifold Σ. The tangential gradient operator ∇_Γ can be transformed into

$$\nabla_\Gamma = \mathbb{T}_\Gamma^{-1} \nabla_\Sigma - \left[\mathbf{n}_\Gamma \cdot \left(\mathbb{T}_\Gamma^{-1} \nabla_\Sigma \right) \right] \mathbf{n}_\Gamma. \tag{11}$$

The unit normal vector on Γ can be transformed into

$$\mathbf{n}_\Gamma^{(d_f)} = \frac{\mathbf{n}_\Sigma - \nabla_\Sigma d_f}{\left\| \mathbf{n}_\Sigma - \nabla_\Sigma d_f \right\|_2}, \tag{12}$$

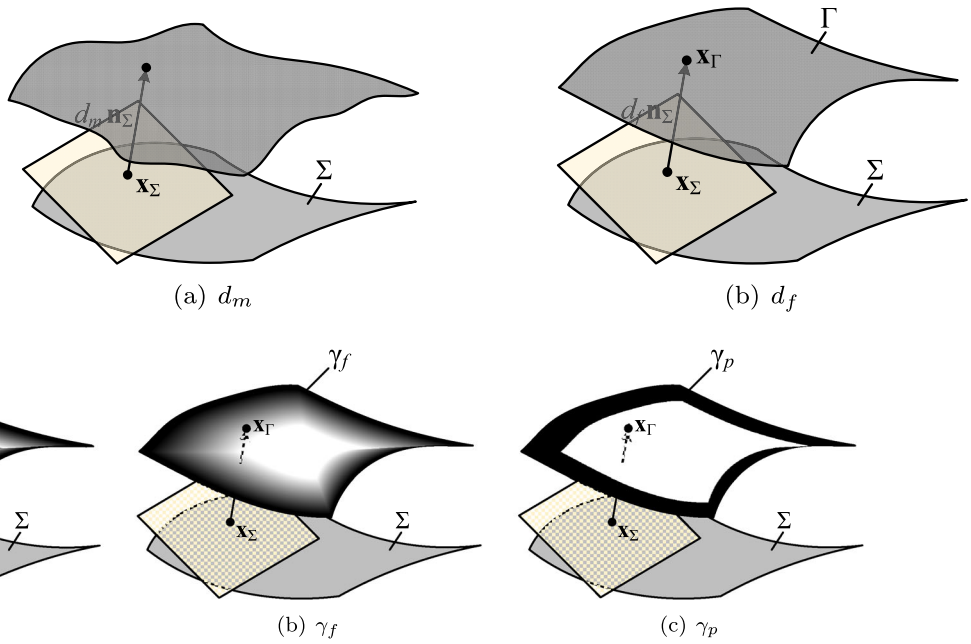

Fig. 3 Sketches for the design variable d_m and the filtered design variable d_f of the implicit 2-manifold Γ defined on the base manifold Σ

Fig. 4 Sketches for the design variable γ, the filtered design variable γ_f and the material density γ_p of the pattern of the surface flow

where $\|\cdot\|_2$ is the 2-norm of a vector. The details for the transformation in Eqs. 11 and 12 are provided in Section S−6.1 of the supplementary material. In Eq. 12, the transformed unit normal vector is distinguished from the original form by using the filtered design variable d_f as the superscript, and this identification method is adopted in the following for the other transformed operators and variables.

Sequentially, the tangential gradient operator ∇_Γ is further transformed into

$$\nabla_\Gamma^{(d_f)} g = \mathbb{T}_\Gamma^{-1}\nabla_\Sigma g - \left[\mathbf{n}_\Gamma^{(d_f)} \cdot \left(\mathbb{T}_\Gamma^{-1}\nabla_\Sigma g\right)\right]\mathbf{n}_\Gamma^{(d_f)},\ \forall g \in \mathcal{H}(\Sigma). \tag{13}$$

Based on the transformed tangential gradient operator, the tangential divergence operator div_Γ can be transformed into

$$\begin{aligned}\mathrm{div}_\Gamma^{(d_f)}\mathbf{g} &= \mathrm{tr}\left(\nabla_\Gamma^{(d_f)}\mathbf{g}\right)\\ &= \mathrm{tr}\left(\mathbb{T}_\Gamma^{-1}\nabla_\Sigma\mathbf{g} - \left[\mathbf{n}_\Gamma^{(d_f)} \cdot \left(\mathbb{T}_\Gamma^{-1}\nabla_\Sigma\mathbf{g}\right)\right]\mathbf{n}_\Gamma^{(d_f)}\right),\ \forall \mathbf{g} \in (\mathcal{H}(\Sigma))^3\end{aligned} \tag{14}$$

where tr is the operator used to extract the trace of a tensor.

The coupling between the design variables plays a crucial role in ensuring numerical stability. Using separate surface-PDE filters for the two design variables introduces different smoothing scales. Therefore, the filter radii must be carefully balanced to prevent numerical oscillations or slow convergence, which may occur if one design variable evolves significantly faster than the other.

2.2.4 Fiber bundle of surface structure

The fiber bundle of the surface structure for mass and heat transfer in surface flow is composed of the base manifold together with the implicit 2-manifold and the pattern of the surface structure, where Σ is the base manifold and $\Gamma \times [0, 1]$ is the fiber, respectively. It can be expressed as

$$\left(\Sigma \times (\Gamma \times [0, 1]), \Sigma, proj_1, \Gamma \times [0, 1]\right), \tag{15}$$

where $proj_1$ is the natural projection $proj_1 : \Sigma \times (\Gamma \times [0, 1]) \to \Sigma$; φ_1 is the homeomorphous map $\varphi_1 : \Sigma \to \Gamma \times [0, 1]$; φ_2 is the homeomorphous map $\varphi_2 : \Gamma \times [0, 1] \to \Sigma \times (\Gamma \times [0, 1])$; and $proj_1$, φ_1 and φ_2 satisfy

$$\begin{cases} proj_1\left(\mathbf{x}_\Sigma, \left(\mathbf{x}_\Gamma, \gamma_p\right)\right) = proj_1\left(\mathbf{x}_\Sigma, \left(d_f\left(\mathbf{x}_\Sigma\right), \gamma_p\right)\right) \\ \quad = \mathbf{x}_\Sigma,\ \forall \mathbf{x}_\Sigma \in \Sigma \\ \varphi_1\left(\mathbf{x}_\Sigma\right) = \left(\mathbf{x}_\Gamma, \gamma_p\right) = \left(d_f\left(\mathbf{x}_\Sigma\right), \gamma_p\right),\ \forall \mathbf{x}_\Sigma \in \Sigma \\ \varphi_2\left(\mathbf{x}_\Gamma, \gamma_p\right) = \left(\mathbf{x}_\Sigma, \left(\mathbf{x}_\Gamma, \gamma_p\right)\right) = \left(\mathbf{x}_\Sigma, \left(d_f\left(\mathbf{x}_\Sigma\right), \gamma_p\right)\right), \\ \quad \forall \left(\mathbf{x}_\Gamma, \gamma_p\right) \in \Gamma \times [0, 1] \end{cases} . \tag{16}$$

The diagram of the fiber bundle in Eq. 15 is shown in Fig. 5.

2.3 Mass transfer problem

The mass transfer process in surface flow can be described by the surface Navier–Stokes equations and the surface convection-diffusion equation.

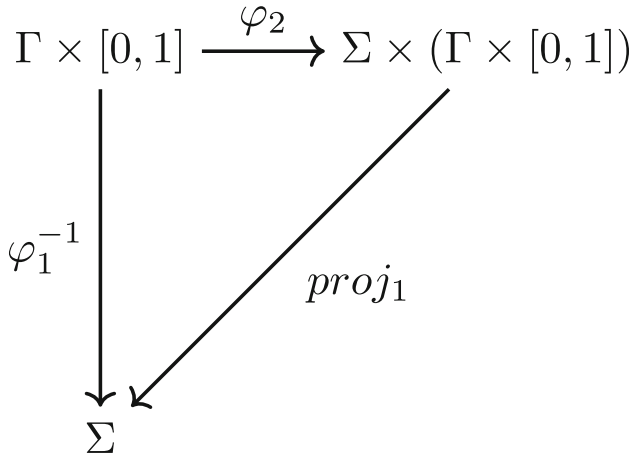

Fig. 5 Diagram for the fiber bundle composed of the base manifold, the implicit 2-manifold and the pattern of the surface structure

2.3.1 Surface Navier–Stokes equations

The governing equations for the motion of a Newtonian surface fluid can be formulated intrinsically on a 2-manifold of codimension one in an Euclidian space. Based on the conservation laws of momentum and mass, the surface Navier–Stokes equations can be derived to describe the incompressible surface flow (Arroyo and DeSimone 2009; Brenner 2013; Rahimi et al. 2013):

$$\left.\begin{aligned} \rho\left(\mathbf{u}\cdot\nabla_\Gamma\right)\mathbf{u} - \mathbb{P}\mathrm{div}_\Gamma\left[\eta\left(\nabla_\Gamma\mathbf{u}+\nabla_\Gamma\mathbf{u}^{\mathrm{T}}\right)\right] + \nabla_\Gamma p &= -\alpha\mathbf{u} \\ -\mathrm{div}_\Gamma\mathbf{u} &= 0 \\ \mathbf{u}\cdot\mathbf{n}_\Gamma &= 0 \end{aligned}\right\} \forall \mathbf{x}_\Gamma \in \Gamma, \tag{17}$$

where $\mathbf{u}$ is the fluid velocity; p is the fluid pressure; ρ is the fluid density; η is the dynamic viscosity; $\mathbf{u}\cdot\mathbf{n}_\Gamma = 0$ is the tangential constraint of the fluid velocity; and $\mathbb{P} = \mathbb{P}(\mathbf{x}_\Gamma) = \mathbb{I} - \mathbf{n}_\Gamma\mathbf{n}_\Gamma^{\mathrm{T}}$ is the normal projector in the tangential space of Γ at $\mathbf{x}_\Gamma$. The tangential constraint is imposed, because the fluid spatially flows on the 2-manifold Γ and the fluid velocity is a vector in the tangential space of Γ.

To solve the mass and heat transfer problem, the fluid velocity and stress in the surface Navier–Stokes equations are required to be specified at the boundaries of the 2-manifold Γ:

$$\begin{cases} \mathbf{u} = \mathbf{u}_{l_{v,\Gamma}},\ \forall \mathbf{x}_\Gamma \in l_{v,\Gamma} \quad \text{(Inlet boundary condition)} \\ \mathbf{u} = \mathbf{0},\ \forall \mathbf{x}_\Gamma \in l_{v_0,\Gamma} \quad \text{(Wall boundary condition)} \\ \left[-\eta\left(\nabla_\Gamma\mathbf{u}+\nabla_\Gamma\mathbf{u}^{\mathrm{T}}\right)+p\mathbb{I}\right]\cdot\mathbf{n}_{\boldsymbol{\tau}_\Gamma} = \mathbf{0},\ \forall \mathbf{x}_\Gamma \in l_{s,\Gamma} \\ \quad \text{(Outlet boundary condition)} \end{cases}, \tag{18}$$

where $\mathbf{u}_{l_{v,\Gamma}}$ is a known distribution of the fluid velocity at the inlet boundary curve of Γ, depending on the specified fluid velocity $\mathbf{u}_{l_{v,\Sigma}}$ at $l_{v,\Sigma}$ representing a boundary curve of Σ; the no-slip boundary condition with velocity equal to $\mathbf{0}$ is imposed on the wall boundary curve $l_{v_0,\Gamma}$ of Γ; and $l_{s,\Gamma}$ is the boundary curve imposed with the outlet boundary condition.

2.3.2 Surface convection-diffusion equation

The mass transfer process in surface flow can be described by the surface convection-diffusion equation defined on the same implicit 2-manifold as the surface Navier–Stokes equations in Section 2.3.1. Based on the conservation law of mass transfer, the surface convection-diffusion equation can be derived to describe the mass transfer process in surface flow (Dziuk and Elliott 2013):

$$\mathbf{u}\cdot\nabla_\Gamma c - \mathrm{div}_\Gamma\left(D\nabla_\Gamma c\right) = 0,\ \forall \mathbf{x}_\Gamma \in \Gamma \tag{19}$$

where c is the mass concentration in the volume flow; and D is the diffusion coefficient. For the surface convection-diffusion equation, the distribution of the concentration is known at the inlet boundary curve $l_{v,\Gamma}$ and the remained part of the boundary curve is insulative:

$$\begin{cases} c = c_0,\ \forall \mathbf{x}_\Gamma \in l_{v,\Gamma} \\ \nabla_\Gamma c\cdot\mathbf{n}_{\boldsymbol{\tau}_\Gamma} = 0,\ \forall \mathbf{x}_\Gamma \in l_{v_0,\Gamma}\cup l_{s,\Gamma} \end{cases} \tag{20}$$

where c_0 is the known distribution of the concentration.

2.3.3 Design objective for mass transfer problem

For mass transfer in surface flow, the desired performance of the surface structure can be set to achieve the anticipated distribution of the concentration at the outlet. The mass transfer performance can be measured by the deviation between the obtained and anticipated distribution of the concentration. Therefore, the design objective of topology optimization on variable 2-manifolds for mass transfer in surface flow is considered as

$$J_c = \int_{l_{s,\Gamma}} (c-\bar{c})^2\ \mathrm{d}l_{\partial\Gamma} \Big/ \int_{l_{v,\Gamma}} (c_0-\bar{c})^2\ \mathrm{d}l_{\partial\Gamma}, \tag{21}$$

where $\bar{c}$ is the anticipated distribution of the concentration at the outlet and it is linearly mapped onto the inlet for the reference value of the concentration deviation.

2.3.4 Constraint of pressure drop

To ensure the patency of the surface structure for mass transfer in surface flow, the constraint of the pressure drop between

the inlet and outlet can be imposed as

$$\left|\Delta P / \Delta P_0 - 1\right| \leq 1 \times 10^{-3}, \tag{22}$$

where ΔP_0 is the specified reference value of the pressure drop and ΔP is the pressure drop between the inlet and outlet:

$$\Delta P = \int_{l_{v,\Gamma}} p \, \mathrm{d}l_{\partial\Gamma} - \int_{l_{s,\Gamma}} p \, \mathrm{d}l_{\partial\Gamma}. \tag{23}$$

2.3.5 Topology optimization problem

Based on the above introduction, the topology optimization problem defined on variable 2-manifolds for mass transfer in surface flow can be constructed to find the optimized matching between the pattern of the surface flow and the implicit 2-manifold, i.e. to optimize the fiber bundle defined in Eq. 15:

$$\begin{cases} \text{Find} \begin{cases} \gamma : \Gamma \to [0,1] \\ d_m : \Sigma \to [0,1] \end{cases} \text{for } (\Sigma \times (\Gamma \times [0,1]), \Sigma, proj_1, \Gamma \times [0,1]), \\ \text{to minimize } \dfrac{J_c}{J_{c,0}} \text{ with } J_c = \displaystyle\int_{l_{s,\Gamma}} (c-\bar{c})^2 \, \mathrm{d}l_{\partial\Gamma} \Big/ \int_{l_{v,\Gamma}} (c_0-\bar{c})^2 \, \mathrm{d}l_{\partial\Gamma}, \\ \text{constrained by} \\ \begin{cases} \begin{cases} \rho (\mathbf{u} \cdot \nabla_\Gamma) \mathbf{u} - \mathbf{P}\mathrm{div}_\Gamma \left[\eta \left(\nabla_\Gamma \mathbf{u} \right.\right. \right. \\ \quad \left.\left.\left. + \nabla_\Gamma \mathbf{u}^{\mathrm{T}}\right)\right] + \nabla_\Gamma p = -\alpha \mathbf{u}, \ \forall \mathbf{x}_\Gamma \in \Gamma \\ -\mathrm{div}_\Gamma \mathbf{u} = 0, \ \forall \mathbf{x}_\Gamma \in \Gamma \\ \mathbf{u} \cdot \mathbf{n}_\Gamma = 0, \ \forall \mathbf{x}_\Gamma \in \Gamma \end{cases} \\ \alpha(\gamma_p) = \alpha_f + (\alpha_s - \alpha_f) q \dfrac{1-\gamma_p}{q+\gamma_p} \end{cases} \\ \mathbf{u} \cdot \nabla_\Gamma c - \mathrm{div}_\Gamma (D \nabla_\Gamma c) = 0, \ \forall \mathbf{x}_\Gamma \in \Gamma \\ \begin{cases} -\mathrm{div}_\Gamma \left(r_f^2 \nabla_\Gamma \gamma_f\right) + \gamma_f = \gamma, \ \forall \mathbf{x}_\Gamma \in \Gamma_D \\ \mathbf{n}_{\boldsymbol{\tau}_\Gamma} \cdot \nabla_\Gamma \gamma_f = 0, \ \forall \mathbf{x}_\Gamma \in \partial\Gamma_D \end{cases} \\ \begin{cases} -\mathrm{div}_\Sigma \left(r_m^2 \nabla_\Sigma d_f\right) + d_f = A_d \left(d_m - \dfrac{1}{2}\right), \ \forall \mathbf{x}_\Sigma \in \Sigma \\ \mathbf{n}_{\boldsymbol{\tau}_\Sigma} \cdot \nabla_\Sigma d_f = 0, \ \forall \mathbf{x}_\Sigma \in \partial\Sigma \end{cases} \\ \Gamma = \left\{\mathbf{x}_\Gamma : \mathbf{x}_\Gamma = d_f \mathbf{n}_\Sigma + \mathbf{x}_\Sigma, \ \forall \mathbf{x}_\Sigma \in \Sigma\right\} \\ \left|\Delta P / \Delta P_0 - 1\right| \leq 1 \times 10^{-3}, \text{ with} \\ \quad \Delta P = \displaystyle\int_{l_{v,\Gamma}} p \, \mathrm{d}l_{\partial\Gamma} - \int_{l_{s,\Gamma}} p \, \mathrm{d}l_{\partial\Gamma} \end{cases} \end{cases} \tag{24}$$

where $J_{c,0}$ is the reference value of the design objective corresponding to the initial distribution of the design variables.

The coupling relations among the variables, functions, tangential divergence operator and tangential gradient operator in Eq. 24 are described as

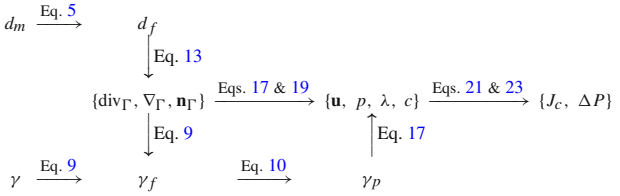

where the design variables d_m and γ are the inputs; the design objective J_c, the pressure drop ΔP and the material density γ_p are the outputs.

2.3.6 Adjoint analysis

The topology optimization problem in Eq. 24 can be solved by using a gradient-based iterative procedure, where the adjoint sensitivities are used to determine the relevant gradient information. The adjoint analysis is implemented for the design objective and pressure drop to derive the adjoint sensitivities. The details for the adjoint analysis have been provided in the supplementary material in Sections S−6.7, S−6.8, S−6.9 and S−6.10 based on the transformation, first order variational and variational formulations of the surface PDEs in Sections S−6.2, S−6.3, S−6.4, S−6.5 and S−6.6.

Based on the transformed design objective and pressure drop in Section S−6.6 of the supplementary material, the adjoint analysis of the topology optimization problem can be implemented on the functional spaces defined on the base manifold. By using the continuous adjoint method (Hinze et al. 2009), the adjoint sensitivity of the design objective J_c is derived as

$$\begin{aligned} \delta J_c = &- \int_{\Sigma_D} \gamma_{fa} \tilde{\gamma} M^{(d_f)} \, \mathrm{d}\Sigma - \int_{\Sigma} A_d d_{fa} \tilde{d}_m \, \mathrm{d}\Sigma, \\ &\forall \tilde{\gamma} \in \mathcal{L}^2(\Sigma_D), \ \forall \tilde{d}_m \in \mathcal{L}^2(\Sigma) \end{aligned} \tag{25}$$

where γ_{fa} and d_{fa} are the adjoint variables of the filtered design variables γ_f and d_f, respectively. The adjoint variables can be derived from the adjoint equations in the variational formulations provided in Section S−6.7 of the supplementary material.

For the constraint of the pressure drop, the adjoint sensitivity of the pressure drop ΔP is derived as

$$\delta\Delta P = -\int_{\Sigma_D} \gamma_{fa}\tilde{\gamma} M^{(d_f)}\,\mathrm{d}\Sigma - \int_{\Sigma} A_d d_{fa}\tilde{d}_m\,\mathrm{d}\Sigma, \quad \forall\tilde{\gamma}\in\mathcal{L}^2(\Sigma_D),\ \forall\tilde{d}_m\in\mathcal{L}^2(\Sigma) \tag{26}$$

where the adjoint variables can be derived from the adjoint equations in the variational formulations provided in Section S−6.9 of the supplementary material.

After the derivation of the adjoint sensitivities in Eqs. 25 and 26, the design variables γ and d_m can be evolved iteratively to determine the fiber bundle of the surface structure for mass transfer in surface flow.

2.4 Heat transfer problem

The heat transfer process in surface flow can be described by the surface Navier–Stokes equations and the surface convective heat-transfer equation, where the surface Navier–Stokes equations used to describe the motion of the surface fluid is the same as that introduced in Section 2.3.1.

2.4.1 Surface convective heat-transfer equation

The heat transfer process in surface flow can be described by the surface convective heat-transfer equation defined on the implicit 2-manifold. Based on the conservation law of energy, the surface convective heat-transfer equation can be derived to describe the heat transfer process in surface flow (Dziuk and Elliott 2013):

$$\rho C_p\mathbf{u}\cdot\nabla_\Gamma T - \mathrm{div}_\Gamma(k\nabla_\Gamma T) = Q,\ \forall\mathbf{x}_\Gamma\in\Gamma \tag{27}$$

where T is the temperature; C_p is the specific heat capacity; k is the coefficient of heat conductivity; and Q is the power of the heat source. For the surface convective heat-transfer equation, the inlet boundary is set as heat sink, i.e. the temperature is known at $l_{v,\Gamma}$; and the remained part of the boundary curves is set to be insulative:

$$\begin{cases} T = T_0,\ \forall\mathbf{x}_\Gamma\in l_{v,\Gamma} \\ \nabla_\Gamma T\cdot\mathbf{n}_{\boldsymbol{\tau}_\Gamma} = 0,\ \forall\mathbf{x}_\Gamma\in l_{v_0,\Gamma}\cup l_{s,\Gamma} \end{cases} \tag{28}$$

where T_0 is the known distribution of the temperature.

The material interpolation in topology optimization on variable 2-manifolds for heat transfer in surface flow is implemented on the specific heat capacity and heat conductivity together with the impermeability of the porous medium in Eq. 4. The specific heat capacity and heat conductivity exist in both the solid and fluid phases. In the solid phase, the convective heat-transfer degenerates into conductive heat transfer, because the fluid velocity is nearly zero in the solid phase of an optimization result; and in the fluid phase, the convective heat-transfer is remained. Therefore, the material interpolations for the specific heat capacity and coefficient of heat conductivity are implemented by using the convex and q-parameterized scheme as

$$\begin{cases} C_p(\gamma_p) = C_{pf} + (C_{ps} - C_{pf})\,q\dfrac{1-\gamma_p}{q+\gamma_p} \\ k(\gamma_p) = k_f + (k_s - k_f)\,q\dfrac{1-\gamma_p}{q+\gamma_p} \end{cases}, \tag{29}$$

where C_{ps} and C_{pf} are the specific heat capacity of the solid and fluid phases, respectively; and k_s and k_f are the coefficients of the heat conductivity of the solid and fluid phases, respectively.

2.4.2 Design objective for heat transfer problem

For heat transfer in surface flow, the desired performance of the surface structure can be set to achieve the minimized thermal compliance. The thermal compliance can be measured by the integration of the square of the temperature gradient in the computational domain. Therefore, the design objective of topology optimization on variable 2-manifolds for heat transfer in surface flow is considered as

$$J_T = \int_\Gamma f_{id,\Gamma} k\nabla_\Gamma T\cdot\nabla_\Gamma T\,\mathrm{d}\Gamma, \tag{30}$$

where J_T is the thermal compliance and $f_{id,\Gamma}$ is the indicator function defined in Eq. 3.

2.4.3 Constraint of dissipation power

To ensure the patency of the surface structure for heat transfer in surface flow, a constraint of the power of the viscous dissipation is imposed and it is expressed as

$$\left|\Phi/\Phi_0 - 1\right| \le 1\times10^{-3}, \tag{31}$$

where Φ_0 is the specified reference value of the dissipation power and Φ is the dissipation power in surface flow:

$$\Phi = \int_\Gamma \frac{\eta}{2}\left(\nabla_\Gamma\mathbf{u} + \nabla_\Gamma\mathbf{u}^{\mathrm{T}}\right) : \left(\nabla_\Gamma\mathbf{u} + \nabla_\Gamma\mathbf{u}^{\mathrm{T}}\right) + \alpha\mathbf{u}^2\,\mathrm{d}\Gamma. \tag{32}$$

2.4.4 Area constraint of surface structure

To regularize the topology optimization problem defined on variable 2-manifolds for heat transfer in surface flow, the area constraint of the surface structure can be imposed as

$$\left|s/s_0 - 1\right| \le 1\times10^{-3}, \tag{33}$$

where s is the area fraction of the surface structure and s_0 is the specified area fraction. The area fraction of the surface structure is defined as

$$s = \frac{1}{|\Gamma_D|}\int_{\Gamma_D} \gamma_p \,\mathrm{d}\Gamma = \frac{1}{|\Gamma_D|}\int_{\Gamma} f_{id,\Gamma}\gamma_p \,\mathrm{d}\Gamma, \tag{34}$$

where $|\Gamma_D|$ is the area of the implicit 2-manifold and it is expressed as

$$|\Gamma_D| = \int_{\Gamma_D} 1 \,\mathrm{d}\Gamma = \int_{\Gamma} f_{id,\Gamma} \,\mathrm{d}\Gamma. \tag{35}$$

2.4.5 Topology optimization problem

Based on the above introduction, the topology optimization problem defined on variable 2-manifolds for heat transfer in surface flow can be constructed to optimize the fiber bundle in Eq. 15:

$$\begin{cases}
\text{Find} \begin{cases} \gamma : \Gamma \to [0,1] \\ d_m : \Sigma \to [0,1] \end{cases} \text{for } (\Sigma \times (\Gamma \times [0,1]), \\
\quad \Sigma, proj_1, \Gamma \times [0,1]), \\
\text{to minimize } \dfrac{J_T}{J_{T,0}} \text{ with } J_T = \displaystyle\int_{\Gamma} f_{id,\Gamma} k \nabla_\Gamma T \cdot \nabla_\Gamma T \,\mathrm{d}\Gamma, \\
\text{constrained by} \\
\quad \begin{cases}
\begin{cases} \rho\left(\mathbf{u}\cdot\nabla_\Gamma\right)\mathbf{u} - \mathbf{P}\mathrm{div}_\Gamma\left[\eta\left(\nabla_\Gamma\mathbf{u} \right.\right. \\ \quad \left.\left. +\nabla_\Gamma\mathbf{u}^{\mathrm{T}}\right)\right] + \nabla_\Gamma p = -\alpha\mathbf{u}, \ \forall \mathbf{x}_\Gamma \in \Gamma \\ -\mathrm{div}_\Gamma\mathbf{u} = 0, \ \forall \mathbf{x}_\Gamma \in \Gamma \\ \mathbf{u}\cdot\mathbf{n}_\Gamma = 0, \ \forall \mathbf{x}_\Gamma \in \Gamma \end{cases} \\
\alpha\left(\gamma_p\right) = \alpha_f + \left(\alpha_s - \alpha_f\right) q \dfrac{1-\gamma_p}{q+\gamma_p}
\end{cases} \\
\quad \begin{cases}
\rho C_p \mathbf{u}\cdot\nabla_\Gamma T - \mathrm{div}_\Gamma\left(k\nabla_\Gamma T\right) = Q, \ \forall \mathbf{x}_\Gamma \in \Gamma \\
\begin{cases} C_p\left(\gamma_p\right) = C_{pf} + \left(C_{ps} - C_{pf}\right) q \dfrac{1-\gamma_p}{q+\gamma_p} \\ k\left(\gamma_p\right) = k_f + \left(k_s - k_f\right) q \dfrac{1-\gamma_p}{q+\gamma_p} \end{cases}
\end{cases} \\
\quad \begin{cases} -\mathrm{div}_\Gamma\left(r_f^2\nabla_\Gamma\gamma_f\right) + \gamma_f = \gamma, \ \forall \mathbf{x}_\Gamma \in \Gamma_D \\ \mathbf{n}_{\boldsymbol{\tau}_\Gamma}\cdot\nabla_\Gamma\gamma_f = 0, \ \forall \mathbf{x}_\Gamma \in \partial\Gamma_D \end{cases} \\
\quad \begin{cases} -\mathrm{div}_\Sigma\left(r_m^2\nabla_\Sigma d_f\right) + d_f = A_d\left(d_m - \dfrac{1}{2}\right), \ \forall \mathbf{x}_\Sigma \in \Sigma \\ \mathbf{n}_{\boldsymbol{\tau}_\Sigma}\cdot\nabla_\Sigma d_f = 0, \ \forall \mathbf{x}_\Sigma \in \partial\Sigma \end{cases} \\
\Gamma = \left\{\mathbf{x}_\Gamma : \mathbf{x}_\Gamma = d_f\mathbf{n}_\Sigma + \mathbf{x}_\Sigma, \ \forall \mathbf{x}_\Sigma \in \Sigma\right\} \\
\left|\Phi/\,\Phi_0 - 1\right| \le 1\times 10^{-3}, \text{ with } \Phi = \displaystyle\int_\Gamma \frac{\eta}{2}\left(\nabla_\Gamma\mathbf{u} + \nabla_\Gamma\mathbf{u}^{\mathrm{T}}\right) : \\
\quad \left(\nabla_\Gamma\mathbf{u} + \nabla_\Gamma\mathbf{u}^{\mathrm{T}}\right) + \alpha\mathbf{u}^2 \,\mathrm{d}\Gamma \\
\left|s/\,s_0 - 1\right| \le 1\times 10^{-3}, \text{ with } s = \dfrac{1}{|\Gamma_D|}\displaystyle\int_{\Gamma_D}\gamma_p \,\mathrm{d}\Gamma \text{ and} \\
\quad |\Gamma_D| = \displaystyle\int_{\Gamma_D} 1 \,\mathrm{d}\Gamma
\end{cases} \tag{36}$$

where $J_{T,0}$ is the reference value of the design objective corresponding to the initial distribution of the design variables.

The coupling relations among the variables, functions, tangential divergence operator and tangential gradient operator in Eq. 36 are illustrated by the arrow chart described as

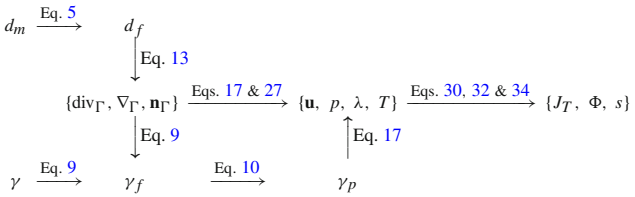

where the design variables d_m and γ, marked in blue, are the inputs; the design objective J_T, the dissipation power Φ and the material density γ_p, marked in red, are the outputs.

2.4.6 Adjoint analysis

To solve the topology optimization problem in Eq. 36 by using a gradient based iterative procedure, the adjoint analysis is implemented for the design objective, dissipation power and area fraction of the surface structure to derive the adjoint sensitivities. The details for the adjoint analysis have been provided in the supplementary material in Sections S−6.14, S−6.15, S−6.16, S−6.17, S−6.18 and S−6.19 based on the transformation, first order variational and variational formulations of the surface PDEs in Sections S−6.2, S−6.3, S−6.11, S−6.12 and S−6.13

Based on the transformed design objective, dissipation power and area fraction in Section S−6.13 of the supplementary material, the adjoint analysis of the topology optimization problem can be implemented on the functional spaces defined on the base manifold. Based on the continuous adjoint method (Hinze et al. 2009), the adjoint sensitivity of the design objective J_T is derived as

$$\begin{aligned} \delta J_T = &-\int_{\Sigma_D} \gamma_{fa}\tilde{\gamma} M^{(d_f)} \,\mathrm{d}\Sigma - \int_{\Sigma} A_d d_{fa}\tilde{d}_m \,\mathrm{d}\Sigma, \\ &\forall\tilde{\gamma} \in \mathcal{L}^2\left(\Sigma_D\right), \ \forall\tilde{d}_m \in \mathcal{L}^2\left(\Sigma\right) \end{aligned} \tag{37}$$

where the adjoint variables can be derived from the adjoint equations in the variational formulations provided in Section S−6.14 of the supplementary material.

For the constraint of the dissipation power, the adjoint sensitivity of the dissipation power Φ is derived as

$$\begin{aligned} \delta\Phi = &-\int_{\Sigma_D} \gamma_{fa}\tilde{\gamma} M^{(d_f)} \,\mathrm{d}\Sigma - \int_{\Sigma} A_d d_{fa}\tilde{d}_m \,\mathrm{d}\Sigma, \\ &\forall\tilde{\gamma} \in \mathcal{L}^2\left(\Sigma_D\right), \ \forall\tilde{d}_m \in \mathcal{L}^2\left(\Sigma\right) \end{aligned} \tag{38}$$

where the adjoint variables can be derived from the adjoint equations in the variational formulations provided in Section S−6.16 of the supplementary material.

For the constraint of the area fraction, the adjoint sensitivity of the area fraction s is derived from that of $s\,|\Gamma_D|$ and $|\Gamma_D|$:

$$\delta s = \delta\left(\frac{s\,|\Gamma_D|}{|\Gamma_D|}\right) = \frac{1}{|\Gamma_D|}\delta\left(s\,|\Gamma_D|\right) - \frac{s}{|\Gamma_D|}\delta\,|\Gamma_D|\,, \tag{39}$$

where the adjoint sensitivities $\delta\left(s\,|\Gamma_D|\right)$ and $\delta\,|\Gamma_D|$ can be derived based on the adjoint analysis of $s^{(d_f)}\,|\Gamma_D|^{(d_f)} = \int_{\Sigma_D}\gamma_p M^{(d_f)}\,\mathrm{d}\Sigma$ and $|\Gamma_D|^{(d_f)} = \int_{\Sigma_D} M^{(d_f)}\,\mathrm{d}\Sigma$. The adjoint sensitivity of $s\,|\Gamma_D|$ is

$$\begin{aligned}\delta\left(s\,|\Gamma_D|\right) = &-\int_{\Sigma_D}\gamma_{fa}\tilde{\gamma}M^{(d_f)}\,\mathrm{d}\Sigma\\ &-\int_{\Sigma}A_d d_{fa}\tilde{d}_m\,\mathrm{d}\Sigma,\ \forall\tilde{\gamma}\in\mathcal{L}^2\left(\Sigma_D\right),\ \forall\tilde{d}_m\in\mathcal{L}^2\left(\Sigma\right)\end{aligned} \tag{40}$$

and the adjoint sensitivity of $|\Gamma_D|$ is

$$\delta\,|\Gamma_D| = \int_{\Sigma} -A_d d_{fa}\tilde{d}_m\,\mathrm{d}\Sigma,\ \forall\tilde{d}_m\in\mathcal{L}^2\left(\Sigma\right) \tag{41}$$

where the adjoint variables can be derived from the adjoint equations in the variational formulations provided in Section S−6.18 of the supplementary material. Then, the adjoint sensitivity of the area fraction in Eq. 39 can be derived based on Eqs. 40 and 41.

After the derivation of the adjoint sensitivities in Eqs. 37, 38 and 39, the design variables γ and d_m can be evolved iteratively to determine the fiber bundle of the surface structure for heat transfer in surface flow.

2.5 Numerical implementation

The topology optimization problems in Eqs. 24 and 36 can be solved by using the iterative algorithms described in Tabs. 1 and 2. The algorithms are implemented in the Matlab environment combined with the finite element software of COMSOL Multiphysics [116,117]. The surface finite element method is utilized to solve the variational formulations of the relevant PDEs and adjoint equations. On the details for the surface finite element solution, one can refer to Ref. (Dziuk and Elliott 2013). Especially, when the surface finite element method is used to solve the surface flow problem on the implicit 2-manifold filled with the porous medium, the Lagrange multiplier method is used to enforce the tangential constraint of the fluid velocity (Fries 2018; Reuther and Voigt 2018). To avoid the numerical singularity caused by the null value, the 2-norm of a vector function $\mathbf{f}$ as the factor of the denominator are approximated as $\left(\mathbf{f}^2+\epsilon_{eps}\right)^{1/2}$, e.g. the 2-norm of $\mathbf{n}_\Sigma-\nabla_\Sigma d_f$ in Eq. 12 and the 2-norm of fluid velocity $\mathbf{u}$ in Eqs. S-124 and S-129 of the supplementary material are numerically approximated as $\left[\left(\mathbf{n}_\Sigma-\nabla_\Sigma d_f\right)^2+\epsilon_{eps}\right]^{1/2}$ and $\left(\mathbf{u}^2+\epsilon_{eps}\right)^{1/2}$, respectively.

In the algorithm for the iterative solution of the topology optimization problem in Eq. 24, the projection parameter β with the initial value of 1 is doubled after the beginning 30 iterations and then doubled after every 20 iterations; the loops of the algorithms are stopped when the maximal iteration numbers are reached, or if β reaching 2^{10}, the averaged variations of the design objectives in continuous 5 iterations and the residuals of the constraints are simultaneously satisfied. In the algorithm for the iterative solution of the topology optimization problem in Eq. 36, the doubling operation of the projection parameter β before it reaching 2^5 can cause significant oscillations of the values of the dissipation power. Therefore, the constraint of the dissipation power can not be well satisfied in the iterative procedure. A bisection method is used to update β and control the amplitude variations of the material density, when β is less than 2^5. The doubling operation is enabled again, when β reaches 2^5. In the algorithms in Tabs. 1 and 2, the design variables are updated by using the method of moving asymptotes (MMA) (Svanberg 1987).

In the algorithms, the constraints in the (n_i)-th iteration are equivalently set as

$$C_{P,n_i}\left|\Delta P_{n_i}/\Delta P_0-1\right|\le 1\times 10^{-3}C_{P,n_i} \tag{42}$$

and

$$\begin{cases} C_{\Phi,n_i}\left|\Phi_{n_i}/\Phi_0-1\right|\le 1\times 10^{-3}C_{\Phi,n_i}\\ C_{s,n_i}\left|s_{n_i}/\,s_0-1\right|\le 1\times 10^{-3}C_{s,n_i}\end{cases} \tag{43}$$

to scale the adjoint sensitivities of the constraints as

$$C_{P,n_i}\delta\Delta P_{n_i} \tag{44}$$

and

$$\begin{cases} C_{\Phi,n_i}\delta\Phi_{n_i}\\ C_{s,n_i}\delta s_{n_i}\end{cases}, \tag{45}$$

where C_{P,n_i}, C_{Φ,n_i} and C_{s,n_i} are the scaling factors. The equivalent operations in Eqs. 42 and 43 can ensure the robust satisfication of the constraints in the iterative procedures, by keeping the adjoint sensitivities of the constraints possess the same magnitude as that of the design objectives. The scaling factors in the (n_i)-th iteration are set as

Table 1 Pseudocodes used to solve the topology optimization problem defined on variable 2-manifolds for mass transfer in surface flow. In the iterative solution loop, n_i is the loop-index; $n_{\max}$ is the maximal value of n_i; J_{c,n_i}, J_{c,n_i-m} and $J_{c,n_i-(m+1)}$ are the values of J_c in the (n_i)-th, (n_i-m)-th and $(n_i-(m+1))$-th iterations, respectively; ΔP_{n_i} is the value of ΔP in the (n_i)-th iteration; C_{c,n_i} is the scaling factor for the adjoint sensitivity of the pressure drop and it is iteratively updated based on Eq. 46; and mod is the operator used to take the remainder

Algorithm 1: iterative solution of Eq. 24

Set $\mathbf{u}_{l_{v,\Sigma}}$, ρ, η, D, c_0, $\bar{c}$, A_d and ΔP_0;
Set $\begin{cases} \gamma \leftarrow 1 \\ d_m \leftarrow 1/2 \end{cases}$, $\begin{cases} r_f = \pi/30 \\ r_m = \pi/4 \end{cases}$, $\begin{cases} n_{\max} \leftarrow 230 \\ n_i \leftarrow 1 \end{cases}$, $\begin{cases} n_{upd} \leftarrow 20 \\ n_{1st} \leftarrow 10 \end{cases}$,
$\begin{cases} \xi \leftarrow 0.5 \\ \beta \leftarrow 1 \end{cases}$, $\begin{cases} \alpha_f \leftarrow 0 \\ \alpha_s \leftarrow 10^4 \rho \end{cases}$, $q \leftarrow 1 \times 10^{-2}$;

for $n_i = 1 : n_{\max}$
  Solve d_f from Eq. 5, and solve γ_f from Eq. 9;
  Project γ_f to derive γ_p based on Eq. 10;
  Solve $\mathbf{u}$, p and λ from Eq. S-82, and evaluate ΔP_{n_i};
  Solve c from Eq. S-87, and evaluate $J_{c,n_i}/J_{c,0}$;
  Solve c_a from Eq. S-90;
  Solve $\mathbf{u}_a$, p_a and λ_a from Eq. S-91;
  Solve γ_{fa} from Eq. S-93, and solve d_{fa} from Eq. S-94;
  Evaluate $\delta J_{c,n_i}$ from Eq. 25;
  Solve $\mathbf{u}_a$, p_a and λ_a from Eq. S-109;
  Solve γ_{fa} from Eq. S-110, and solve d_{fa} from Eq. S-94;
  Evaluate $\delta \Delta P_{n_i}$ from Eq. 26;
  Update γ and d_m based on $\delta J_{c,n_i}$ and $C_{P,n_i}\delta \Delta P_{n_i}$ by using MMA;
  if $(n_i == n_{upd} + n_{1st}) \vee ((n_i > n_{upd} + n_{1st}) \wedge (\mathrm{mod}\,(n_i - n_{upd} - n_{1st}, n_{upd}) == 0))$
    $\beta \leftarrow 2\beta$;
  end if
  if $(n_i == n_{\max}) \vee \begin{cases} \beta == 2^{10} \\ \frac{1}{5}\sum_{m=0}^{4} \left| J_{c,n_i-m} - J_{c,n_i-(m+1)} \right| / J_{c,0} \le 1 \times 10^{-3} \\ |\Delta P_{n_i}/\Delta P_0 - 1| \le 1 \times 10^{-3} \end{cases}$
    break;
  end if
  $n_i \leftarrow n_i + 1$
end for

$$C_{P,n_i} = \frac{\Delta P_0}{J_{c,0}} \left\| \frac{\Delta J_{c,n_i}}{\Delta \boldsymbol{\Upsilon}} \right\|_2 \Big/ \left\| \frac{\Delta \Delta P_{n_i}}{\Delta \boldsymbol{\Upsilon}} \right\|_2 \tag{46}$$

and

$$\begin{cases} C_{\Phi,n_i} = \dfrac{\Phi_0}{J_{T,0}} \left\| \dfrac{\Delta J_{T,n_i}}{\Delta \boldsymbol{\Upsilon}} \right\|_2 \Big/ \left\| \dfrac{\Delta \Phi_{n_i}}{\Delta \boldsymbol{\Upsilon}} \right\|_2 \\ C_{s,n_i} = \dfrac{s_0}{J_{T,0}} \left\| \dfrac{\Delta J_{T,n_i}}{\Delta \boldsymbol{\Upsilon}} \right\|_2 \Big/ \left\| \dfrac{\Delta s_{n_i}}{\Delta \boldsymbol{\Upsilon}} \right\|_2 \end{cases}, \tag{47}$$

where

$$\left\{ \Delta J_{c,n_i} \big/ \Delta \boldsymbol{\Upsilon}, \Delta \Delta P_{n_i} \big/ \Delta \boldsymbol{\Upsilon} \right\}, \tag{48}$$

$$\left\{ \Delta J_{T,n_i} \big/ \Delta \boldsymbol{\Upsilon}, \Delta \Phi_{n_i} \big/ \Delta \boldsymbol{\Upsilon} \right\} \tag{49}$$

and

$$\left\{ \Delta J_{T,n_i} \big/ \Delta \boldsymbol{\Upsilon}, \Delta s_{n_i} \big/ \Delta \boldsymbol{\Upsilon} \right\} \tag{50}$$

are the discretized counterparts of

$$\left\{ \delta J_{c,n_i} \big/ \delta \gamma, \delta \Delta P_{n_i} \big/ \delta \gamma \right\}, \tag{51}$$

$$\left\{ \delta J_{T,n_i} \big/ \delta \gamma, \delta \Phi_{n_i} \big/ \delta \gamma \right\} \tag{52}$$

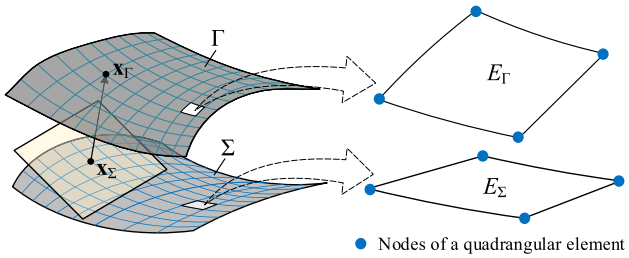

Fig. 6 Sketch for the meshes of the quadrangular-element based discretization of the base manifold Σ and the mapped meshes on the implicit 2-manifold Γ

and

$$\left\{ \delta J_{T,n_i} \big/ \delta \gamma, \delta s_{n_i} \big/ \delta \gamma \right\}. \tag{53}$$

Linear quadrangular elements are used to interpolate the design variable of the surface structure and that of the implicit 2-manifold, and solve the variational formulations of the governing equations, the surface-PDE filters and the adjoint equations. The meshes of the quadrangular-element based discretization of the base manifold have been sketched in Fig. 6, including the mapped meshes on the implicit 2-manifold.

Table 2 Pseudocodes used to solve the topology optimization problem defined on variable 2-manifolds for heat transfer in surface flow. In the iterative solution loop, $\|\cdot\|_\infty$ represents the ∞-norm of a function and its discrete counterpart is the maximal component of the absolute of the discretized function; J_{T,n_i}, J_{T,n_i-m} and $J_{T,n_i-(m+1)}$ are the values of J_T in the (n_i)-th, (n_i-m)-th and $(n_i-(m+1))$-th iterations, respectively; Φ_{n_i} and s_{n_i} are the values of Φ and s in the (n_i)-th iteration; C_{T,n_i} is the scaling factor for the adjoint sensitivities of the dissipation power and area fraction, and they are iteratively updated based on Eq. 47

Algorithm 2: iterative solution of Eq. 36

Set $\mathbf{u}_{l_{v,\Sigma}}$, ρ, η, T_0, A_d, Φ_0 and s_0;

Set $\begin{cases} \gamma \leftarrow 1/2 \\ d_m \leftarrow 1/2 \end{cases}$, $\begin{cases} r_f = \pi/30 \\ r_m = \pi/4 \end{cases}$, $\begin{cases} n_i \leftarrow 1 \\ n_{2^{10}} \leftarrow 0 \end{cases}$, $\begin{cases} n_{upd} \leftarrow 20 \\ n_{1st} \leftarrow 10 \end{cases}$, $\begin{cases} \xi \leftarrow 0.5 \\ \beta \leftarrow 1 \end{cases}$, $\begin{cases} \beta' \leftarrow 0 \\ \gamma'_p \leftarrow 0 \end{cases}$, $\begin{cases} \alpha_f \leftarrow 0 \\ \alpha_s \leftarrow 10^4\rho \end{cases}$, $\begin{cases} C_{pf} \leftarrow 1\times10^{0} \\ C_{ps} \leftarrow 1\times10^{-1} \end{cases}$, $\begin{cases} k_f \leftarrow 1\times10^{-1} \\ k_s \leftarrow 1\times10^{0} \end{cases}$, $q \leftarrow 1\times10^{-2}$, $\epsilon_{\gamma_p} \leftarrow 5\times10^{-2}$;

while $\beta \le 2^{10}$
  Solve d_f from Eq. 5, and solve γ_f from Eq. 9;
  if $(n_i \ge n_{upd}+n_{1st}) \wedge (\mathrm{mod}(n_i - n_{upd} - n_{1st}, n_{upd}) == 1)$
    Compute γ_p from γ_f based on Eq. 10;
    if $\beta < 2^5$
      $n_{2^5} \leftarrow 0$; $\beta' \leftarrow 2\beta$;
      Compute γ'_p from γ_f based on Eq. 10 with γ_p and β replaced to be γ'_p and β';
      while $\|\gamma'_p - \gamma_p\|_\infty \ge \epsilon_{\gamma_p}$
        $\beta' \leftarrow (\beta'+\beta)/2$;
        Compute γ'_p from γ_f based on Eq. 10 with γ_p and β replaced to be γ'_p and β';
      end while
      $\beta \leftarrow \beta'$;
    else
      if $n_{2^5} == 1$
        $\beta \leftarrow 2\beta$;
      elseif $n_{2^5} == 0$
        $\beta \leftarrow 2^5$; $n_{2^5} \leftarrow 1$;
      end if
    end if
    if $\beta == 2^{10}$
      $n_{2^{10}} \leftarrow n_{2^{10}} + 1$;
    end if
    if $\big((\beta == 2^{10}) \wedge \big(\frac{1}{5}\sum_{m=0}^{4} |J_{T,n_i-m} - J_{T,n_i-(m+1)}| / J_{T,0} \le 1\times10^{-3}\big)$
      $\wedge \big(|\Phi_{n_i}/\Phi_0 - 1| \le 1\times10^{-3}\big) \wedge \big(|s_{n_i}/s_0 - 1| \le 1\times10^{-3}\big)\big) \vee (n_{2^{10}} == n_{upd})$
      break;
    end if
  end if
  Project γ_f to derive γ_p based on Eq. 10;
  Solve $\mathbf{u}$, p and λ from Eq. S-125, and evaluate Φ_{n_i};
  Solve T from Eq. S-130, and evaluate $J_{T,n_i}/J_{T,0}$;
  Solve T_a from Eq. S-135, and solve $\mathbf{u}_a$, p_a and λ_a from Eq. S-136;
  Solve γ_{fa} from Eq. S-138, and solve d_{fa} from Eq. S-139;
  Evaluate $\delta J_{T,n_i}$ from Eq. 37;
  Solve $\mathbf{u}_a$, p_a and λ_a from Eq. S-151;
  Solve γ_{fa} from Eq. S-152, and solve d_{fa} from Eq. S-153;
  Evaluate $\delta\Phi_{n_i}$ from Eq. 38;
  Solve γ_{fa} from Eq. S-163, and solve d_{fa} from Eq. S-164;
  Evaluate $\delta\left(s|\Gamma|\right)_{n_i}$ from Eq. 40;
  Solve d_{fa} from Eq. S-165;
  Evaluate $\delta|\Gamma|_{n_i}$ from Eq. 41;
  Evaluate δs_{n_i} from $\delta\left(s|\Gamma|\right)_{n_i}$ and $\delta|\Gamma|_{n_i}$ from Eq. 39;
  Update γ and d_m based on $\delta J_{T,n_i}$, $C_{\Phi,n_i}\delta\Phi_{n_i}$ and $C_{s,n_i}\delta s_{n_i}$ by using MMA;
  $n_i \leftarrow n_i + 1$;
end while

3 Results and discussion

For topology optimization on variable 2-manifolds for mass and heat transfer in surface flow, the design domains are shown in Fig. 7 with initial designs shown in Fig. 8, including a series of curved surfaces obtained by deforming a flat surface into cylindrical surfaces, where the lengths of the inlet, outlet and wall boundaries are remained to be unchanged during the deformation. The flat surface is a rectangle with the lengths of the inlet and outlet equal to π, the length of computational domain equal to 4π and the length of design domain equal to 2π. In the numerical computation, the design domains are discretized by using the curved quadrilateral element with the side length of $\pi/60$. The filter radii of the design variables for the implicit 2-manifolds and patterns of the surface flow are set to be $\pi/30$ and $\pi/4$, respectively.

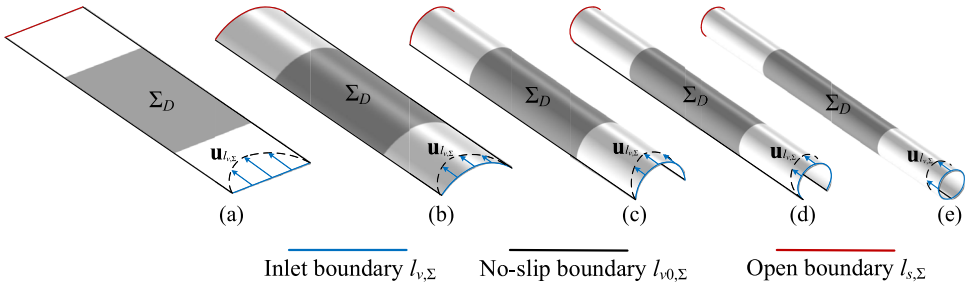

Fig. 7 Design domains of topology optimization on variable 2-manifolds for mass and heat transfer in surface flow

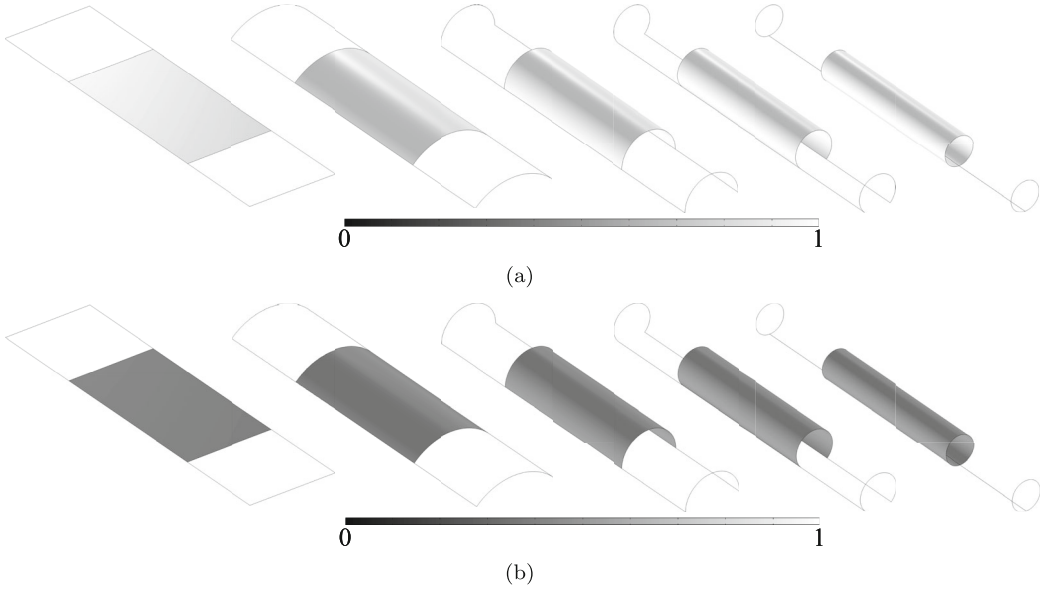

Fig. 8 Initial designs for topology optimization on variable 2-manifolds for mass and heat transfer in surface flow. (a) Initial designs for mass transfer, where the design variables are set as $\gamma = 1$ and $d_m = 0$; (b) initial design for heat transfer, where the design variables are set as $\gamma = 0.5$ and $d_m = 0$

3.1 Mass transfer in surface flow

In topology optimization on variable 2-manifolds for mass transfer in surface flow, the fluid density and viscosity are set as the unitary, the diffusion coefficient is set as $D = 5\times10^{-3}$, the optimization parameters in the material interpolation are set as $\alpha_s = 1\times10^{4}$ and $q = 1\times10^{-2}$, the pressure drop is set as $\Delta P_0 = 1.5\times10^{3}$, the inlet velocity is set as the parabolic distribution with the maximal value of 1, and the concentration distribution at the inlet is set by using the step function with the mid-value at the central point of the inlet boundary and the maximal and minimal values of 2 and 0. Correspondingly, the anticipated distribution of the concentration at the outlet is $\bar{c} = 1$. By setting the variable magnitude of the implicit 2-manifold as 1.0, the topology optimization problem in Eq. 24 is solved on the design domains shown in Fig. 7. The distribution of the filtered design variables for the implicit 2-manifolds and the material density for the patterns are obtained as shown in Fig. 9, where the fiber bundles composed of the implicit 2-manifolds and the surface patterns are included. Convergent histories of the design objective and constraint of the pressure drop are plotted in Fig. 10 for topology optimization on the design domain in Fig. 7c, including snapshots for the evolution of the fiber bundle during the iterative solution of the optimization problem. From the monotonicity of the objective values and satisfaction of the constraint of the pressure drop, the robustness of the iterative solution can be confirmed for the topology optimization procedure. The distribution of the velocity, pressure and concentration are provided in Fig. 11 for topology optimization on the design domain in Fig. 7c, where the zig-zag shaped curved-channel is obtained for the surface flow to enhance the convection and mixing length and hence the mass-transfer efficiency is improved.

The variable magnitude of the implicit 2-manifold can affect the design space of the topology optimization problem. Therefore, the topology optimization problem is solved for the variable magnitudes of

$$A_d = \{0.0, 0.5, 1.0, 1.5, 2.0\}\,, \tag{54}$$

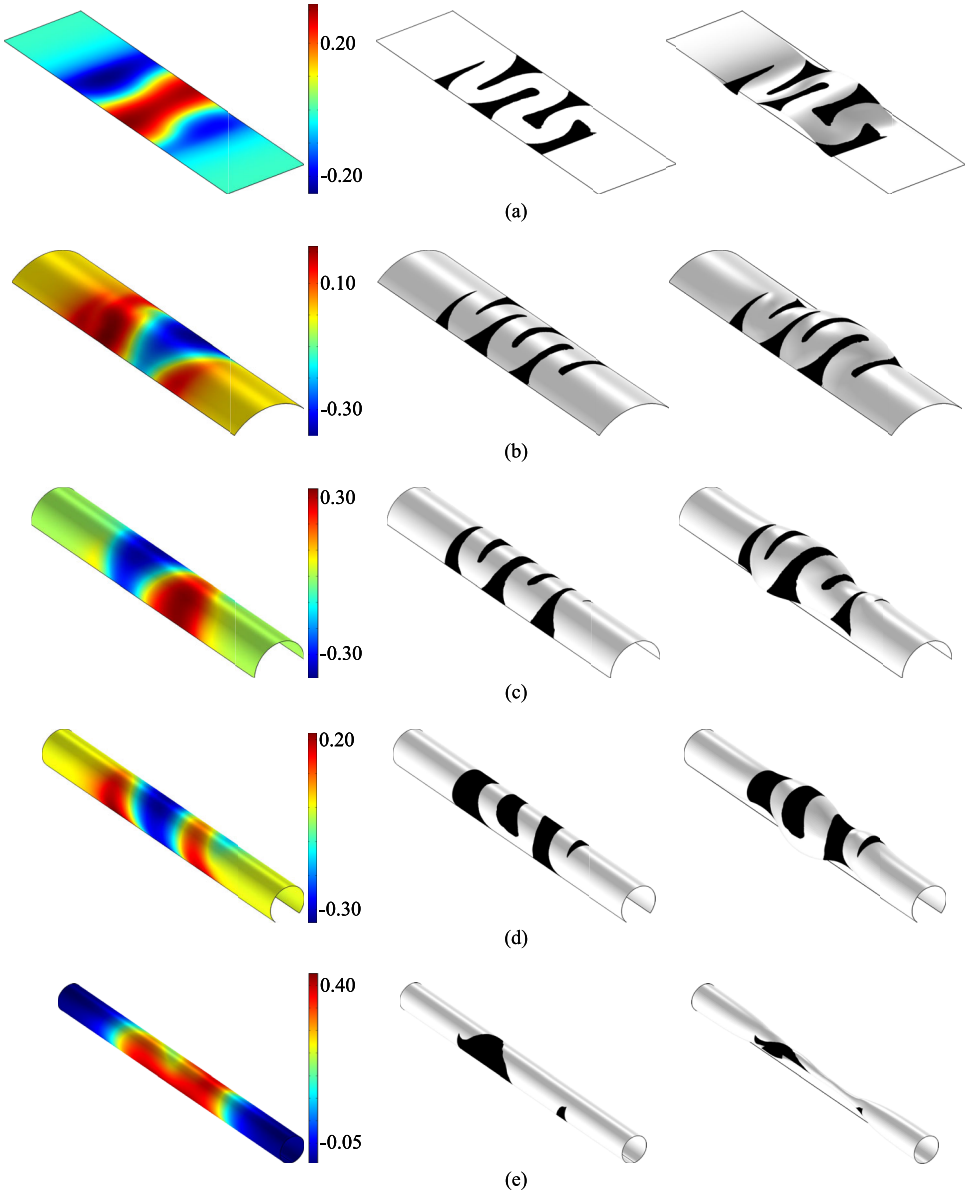

Fig. 9 Distribution of the normal displacement for the implicit 2-manifolds and the material density for the surface patterns obtained for mass transfer in the surface flow on the design domains sketched in Fig. 7, including the fiber bundles composed of the base manifold and the surface patterns defined on the implicit 2-manifolds. The legend is the value of the filtered design variable of the implicit 2-manifolds. It ranges from negative to positive, because the variable magnitude in Eq. 5 is values from $-A_d/2$ to $A_d/2$

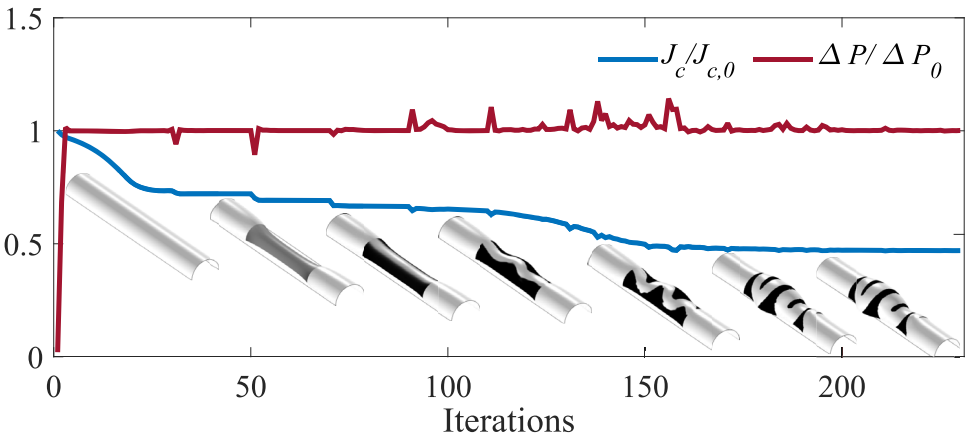

Fig. 10 Convergent histories of the design objective and constraint of the pressure drop for mass transfer in the surface flow on the design domain sketched in Fig. 7c, including the snapshots for the evolution of the fiber bundle during the iterative solution of the optimization problem

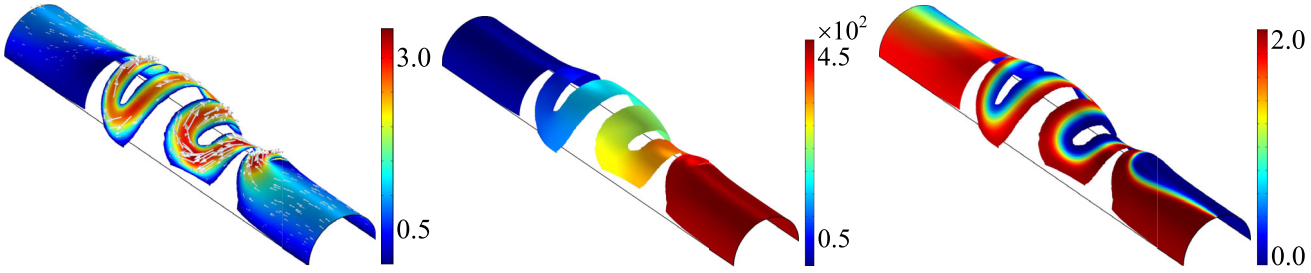

(a) Velocity (b) Pressure (c) Concentration

Fig. 11 Distribution of the velocity, pressure and concentration on the fiber bundle obtained for mass transfer in the surface flow on the design domain sketched in Fig. 7c

where the other parameters are remained to be unchanged. The values of the design objective are obtained and plotted in Fig. 12 including the obtained fiber bundles. Fig. 12 shows that the objective values decrease along with increasing the variable magnitude. This is because that larger variable magnitude permits more flexible evolution of the fiber bundle to improve the mixing performance of the surface structure. Especially, the objective value is less than 0.05 when the variable magnitude is $A_d = 2.0$. This means that the complete mixing is achieved by the surface structure corresponding to the fiber bundle with the variable magnitude of $A_d = 2.0$.

Reynolds number can be used to characterize the relative dominance of the convection and viscosity in surface flow. It can be defined as

$$Re = \frac{\rho \sup_{\forall \mathbf{x}_\Gamma \in l_{v,\Gamma}} \left\| \mathbf{u}_{l_{v,\Gamma}} \right\|_2 \left| l_{v,\Gamma} \right|}{\eta} \tag{55}$$

where $\sup_{\forall \mathbf{x}_\Gamma \in l_{v,\Gamma}} \left\| \mathbf{u}_{l_{v,\Gamma}} \right\|_2$ is the maximal value of the inlet velocity and $\left| l_{v,\Gamma} \right|$ is the length of the inlet boundary. Then, the topology optimization problem is solved for the Reynolds numbers of

$$Re = \left\{ 10^{-1}\pi, 10^{-1/2}\pi, 10^{0}\pi, 10^{1/2}\pi, 10^{1}\pi \right\}, \tag{56}$$

where the other parameters are remained to be unchanged. The values of the design objective are obtained and plotted in Fig. 13 including the obtained fiber bundles. Fig. 13 shows that the objective values increase along with increasing the Reynolds number. This is because that larger Reynolds number means larger fluid velocity and shorter mixing time during the fluid flowing through the surface structure. At low Reynolds number, relatively thin surface structures are obtained to satisfy the constraint of the pressure drop. They become thick along with the increase of the Reynolds number, because higher Reynolds number increases the pressure drop and the surface structure needs to be thick enough to decrease the pressure drop and satisfy the corresponding constraint.

Péclet number can be used to characterize the relative dominance of the convection and diffusion in the mass transfer process. It can be defined as

$$Pe = \frac{\sup_{\forall \mathbf{x}_\Gamma \in l_{v,\Gamma}} \left\| \mathbf{u}_{l_{v,\Gamma}} \right\|_2 \left| l_{v,\Gamma} \right|}{D}. \tag{57}$$

Then, the topology optimization problem is solved for the Péclet numbers of

$$Pe = \left\{ 1 \times 10^2\pi, 2 \times 10^2\pi, 3 \times 10^2\pi, 4 \times 10^2\pi, 5 \times 10^2\pi \right\} \tag{58}$$

where the other parameters are remained to be unchanged. The values of the design objective are obtained and plotted in Fig. 14 including the obtained fiber bundles. Fig. 14 shows that the objective values increase along with increasing the Péclet number. This is because that larger Péclet number means the dominance of the convection becomeing stronger and the mixing time being equivalently reduced in the surface structure.

The constraint of the pressure drop can be used to ensure the smoothness of surface flow. Based on the results in Fig. 12, it is investigated for the variable magnitudes of $A_d = \{1.0, 1.5, 2.0\}$ on the design domain in Fig. 7c. For the variable magnitude of $A_d = 1.0$, the topology optimization problem is solved for different values of the pressure drop and the objective values are plotted in Fig. 15a including the obtained fiber bundles. In Fig. 15a, there is a transition of the monotonicity of the objective values at the pressure drop of 4×10^3. The transition shows that reasonable increase of the pressure drop can improve the mixing performance of the surface structures. This is because that reasonable increase of the pressure drop can enhance the convection of surface flow and mixing efficiency can be improved by the enhanced convection. However, the pressure drop can not be increased consistently, because too large pressure drop causes the thin surface structures and large fluid velocity and this equivalently increases the mixing length. When the vari-

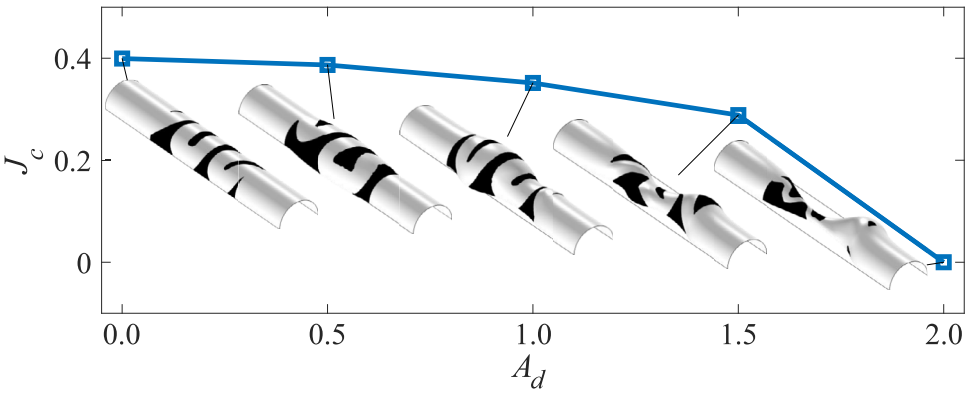

Fig. 12 Objective values for the variable magnitudes of $A_d = \{0.0, 0.5, 1.0, 1.5, 2.0\}$ and the obtained fiber bundles for mass transfer in the surface flow

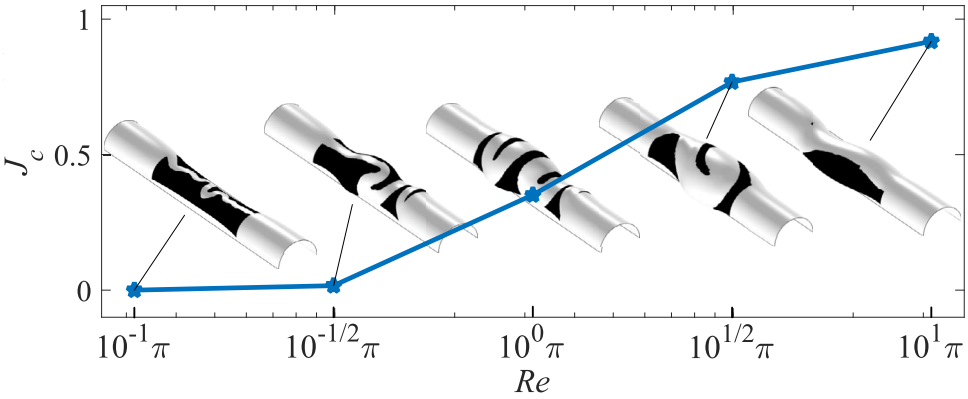

Fig. 13 Objective values for the Reynolds numbers of $Re = \{10^{-1}\pi, 10^{-1/2}\pi, 10^{0}\pi, 10^{1/2}\pi, 10^{1}\pi$ and the obtained fiber bundles for mass transfer in surface flow

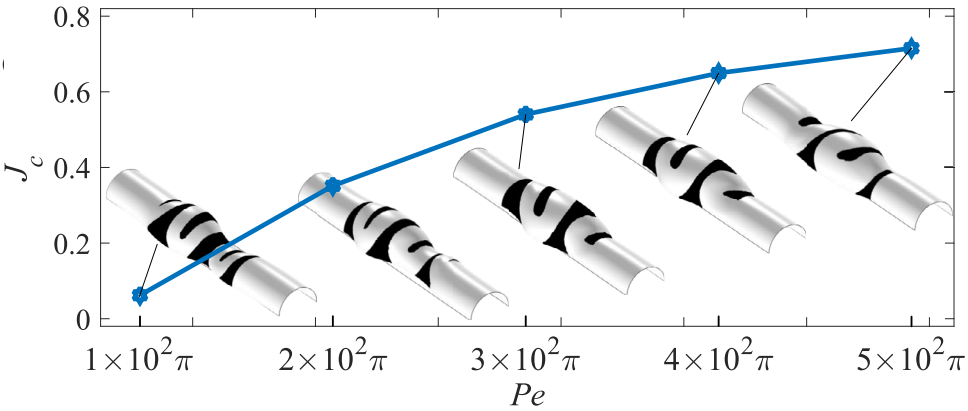

Fig. 14 Objective values for the Péclet numbers of $Pe = \{1 \times 10^2\pi, 2 \times 10^2\pi, 3 \times 10^2\pi, 4 \times 1$ and the obtained fiber bundles for mass transfer in surface flow

able magnitude is increased to $A_d = 1.5$ and $A_d = 2.0$, the transition of the monotonicity of the objective values disappears as shown in Figs. 15b and 15c. This is because that the mixing mode is changed after a critical value of the pressure drop. When the pressure drop arrives at the critical value, the vortex based mixing modes appear as shown in Fig. 16, where vortexes are generated on the implicit 2-manifolds, the convection is enhanced effectively and the mixed fluid around the interfaces of two solutions is extracted by a thin surface channel connected to the interface of the vortexes. The vortex based mixing modes can achieve complete mixing as shown in Fig. 16. Therefore, the increase of the pressure drop can achieve complete mixing by inducing vortex based mixing modes, when the variable magnitude is preset to be large enough in the topology optimization problem.

To confirm the optimality, the results in Fig. 14 are cross-compared by computing the objective values for the obtained fiber bundles at different Péclet numbers, where the Reynolds number is kept as $10^0\pi$. The computed objective values are listed in Tab. 3. From the comparison of the objective values in every row of Tab. 3, the optimized performance of the obtained fiber bundles can be confirmed.

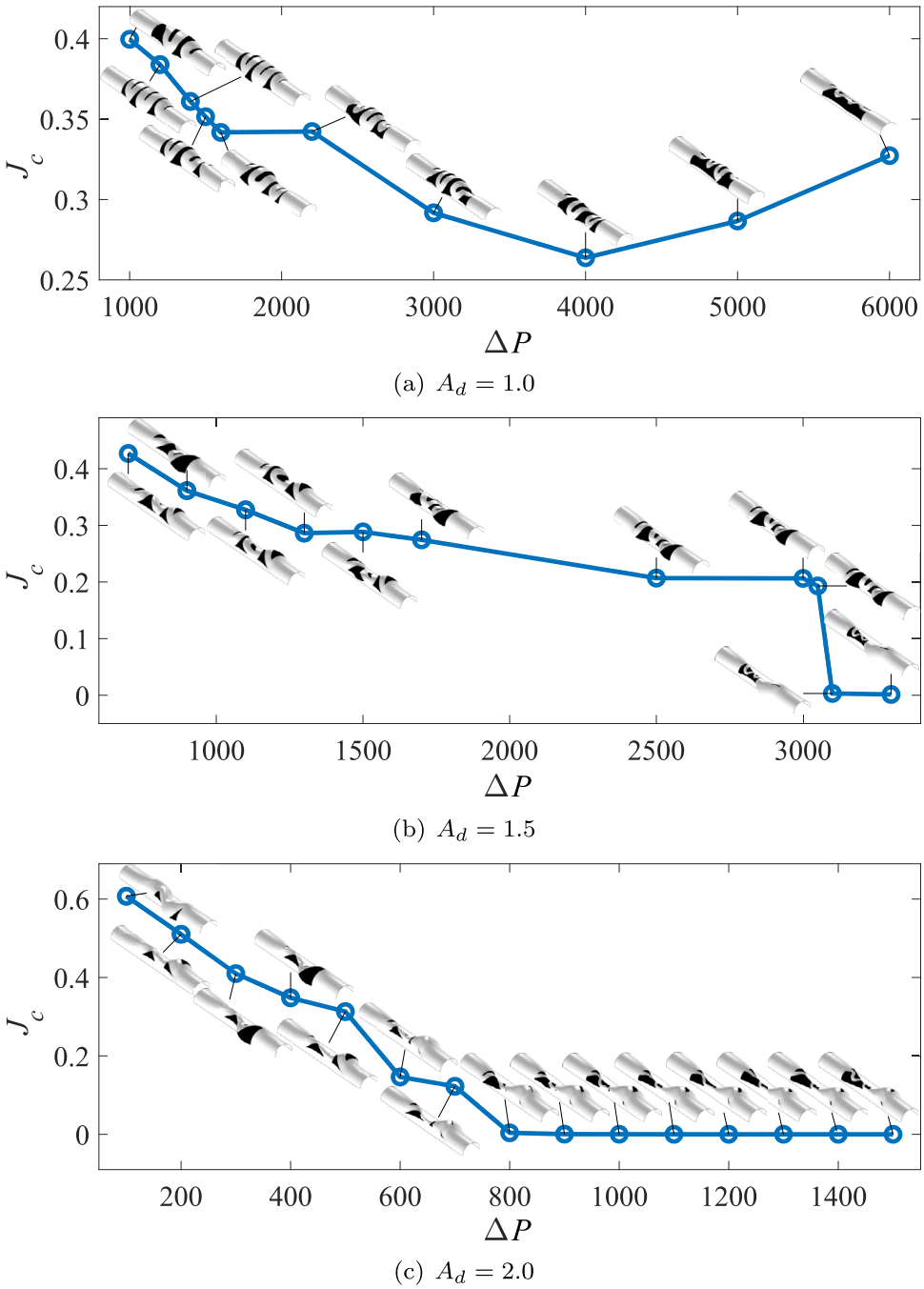

Fig. 15 Objective values and the obtained fiber bundles for different pressure drop for mass transfer in surface flow

3.2 Heat transfer in surface flow

In topology optimization on variable 2-manifolds for heat transfer in surface flow, the fluid density and viscosity are also considered as unitary. The material coefficients and optimization parameters are set as that in Tab. 2. The inlet velocity is set as the parabolic distribution with the maximal value of 1, and the temperature distribution at the inlet is set to be homogeneous with the unitary value. By setting the variable magnitude as 1.5, the topology optimization problem in Eq. 36 is solved on the design domains in Fig. 7. The distribution of the filtered design variables for the implicit 2-manifolds and the material density for the patterns are obtained as shown in Fig. 17, where the fiber bundles composed of the implicit 2-manifolds and the surface patterns are included. Convergent histories of the optimization objective and constraints of the dissipation power and area fraction are plotted in Fig. 18 for topology optimization on the design domain in Fig. 17c, including snapshots for the evolution of the fiber bundle during the iterative solution of the optimization problem.

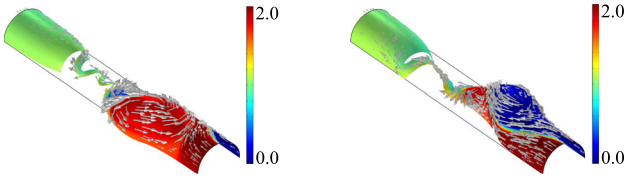

(a) $A_d = 1.5, \Delta P = 3100$ (b) $A_d = 2.0, \Delta P = 800$

Fig. 16 Concentration distribution in the vortex based mixing modes on the topologically optimized fiber bundles

From the monotonicity of the objective values and satisfication of the constraints of the dissipation power and area fraction, the robustness of the iterative procedure can be confirmed for topology optimization for heat transfer in surface flow. The distribution of the velocity, pressure and temperature are provided in Fig. 19 for topology optimization on the design domain in Fig. 7c, where the splitting-merging shaped curved-channel is obtained for the surface flow to enhance the convection, enlarge the diffusion length, decrease the surface gradient of the temperature distribution and the efficiency of heat transfer is thereby improved.

The variable magnitudes of

$$A_d = \{0.0, 0.5, 1.0, 1.5, 2.0\} \tag{59}$$

are investigated for topology optimization of heat transfer in surface flow, where the other parameters are remained to be unchanged. The values of the design objective are obtained and plotted in Fig. 20 including the obtained fiber bundles. Because larger variable magnitude permits more flexible evolution of the fiber bundle to improve the heat transfer performance of the surface structure, the objective values in Fig. 20 decrease along with increasing the variable magnitude.

To investigate the effect of the Reynolds number defined in Eq. 55, the topology optimization problem for heat transfer in surface flow is solved for the Reynolds numbers of

$$Re = \left\{10^{-1}\pi, 10^{-1/2}\pi, 10^{0}\pi, 10^{1/2}\pi, 10^{1}\pi\right\}, \tag{60}$$

where the other parameters are remained to be unchanged. The values of the design objective are obtained and plotted in Fig. 21 including the obtained fiber bundles. To remain the Péclet number to be unchanged in the investigation of the Reynolds number, the dynamic viscosity of the fluid is changed, where high Reynolds number corresponds to low dynamic viscosity. Because the specified value of the dissipation power is remained to be unchanged, splitting-merging shape of the curved channel and decrease of the width of the channel can help to ensure the satisfication of the constraint of the dissipation power in the surface flow with high Reynolds number and low dynamic viscosity. Simultaneously, this can improve the heat transfer performance by decreasing the surface gradient of the temperature distribution. Therefore, the objective values decrease along with increasing the Reynolds number in Fig. 21.

In the convective heat-transfer problem, Péclet number is used to characterize the relative dominance of the convection and thermal conductivity. It can be defined as

$$Pe = \frac{\rho C_{pf} \sup_{\forall \mathbf{x}_\Gamma \in l_{v,\Gamma}} \left\| \mathbf{u}_{l_{v,\Gamma}} \right\|_2 \left| l_{v,\Gamma} \right|}{k_f}. \tag{61}$$

Then, the topology optimization problem is solved for the Péclet numbers of

$$Pe = \left\{10^{-1}\pi, 10^{0}\pi, 10^{1}\pi, 10^{2}\pi, 10^{3}\pi\right\}, \tag{62}$$

where the other parameters are remained to be unchanged. The values of the design objective are obtained and plotted in Fig. 22 including the obtained fiber bundles. To remain the Reynolds number to be unchanged in the investigation of the Péclet number, the thermal conductivity of the fluid is changed, where high Péclet number corresponds to small coefficient of the thermal conductivity. Because both thermal conductivity and convection are helpful for the improvement of the heat transfer performance, there is a joint point of those two factors when the Péclet number is changed. Therefore, the obtained fiber bundle at the Péclet number of $10^1\pi$ has the lowest value of the design objective. This is achieved by the splitting-merging shape of the curved channel together with the thermal conductivity of the fluid, where the convection of the surface flow is enhanced by the splitting-merging shape.

The constraint of the dissipation power can be used to ensure the smoothness of surface flow. Based on the results in Fig. 23, it is investigated for the variable magnitude of $A_d = 1.5$ on the design domain in Fig. 7c. The topology optimization problem is solved for different values of the specified dissipation power and the objective values are plotted in Fig. 23 including the obtained fiber bundles. When the dissipation power is specified with a large value, more blocks are presented and the width of the fluid channel becomes thin to enlarge the gradient of the fluid velocity and satisfy the constraint of the dissipation power. Then, the convection of the surface flow is enhanced and the heat transfer performance is improved. Therefore, the objective values in Fig. 23 decrease along with the increase of the specified values of the dissipation power.

To confirm the optimality, the results in Fig. 22 are cross-compared by computing the objective values for the obtained fiber bundles at different Péclet numbers, where the Reynolds number is kept as $10^0\pi$. The computed objective values are listed in Tab. 4. From the comparison of the objective values in every row of Tab. 4, the optimized performance of the obtained fiber bundles can be confirmed.

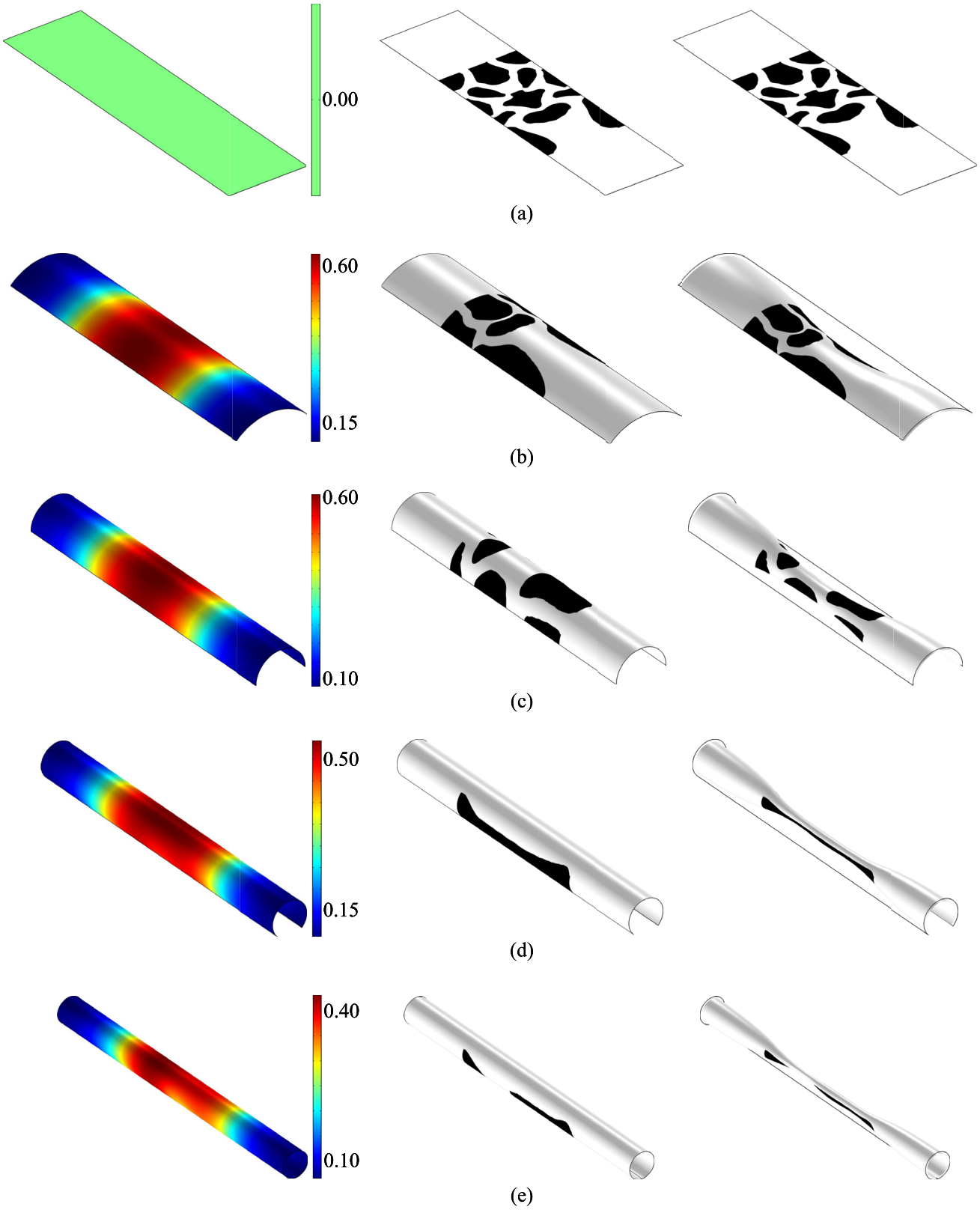

Fig. 17 Distribution of the normal displacement for the implicit 2-manifolds and the material density of the surface patterns for heat transfer in the surface flow on the design domains sketched in Fig. 7, including the fiber bundles composed of the implicit 2-manifolds and the surface patterns

Table 3 Objective values for the obtained fiber bundle in Fig. 14 at different Péclet numbers, where the Reynolds number is kept as $10^0\pi$

	 $Pe = 1 \times 10^2\pi$	 $Pe = 2 \times 10^2\pi$	 $Pe = 3 \times 10^2\pi$	 $Pe = 4 \times 10^2\pi$	 $Pe = 5 \times 10^2\pi$
$Pe = 1 \times 10^2\pi$	**0.0621**	0.6243	0.6491	0.6548	0.6419
$Pe = 2 \times 10^2\pi$	0.7640	**0.3515**	0.7763	0.7789	0.7700
$Pe = 3 \times 10^2\pi$	0.8156	0.8125	**0.5402**	0.8269	0.8197
$Pe = 4 \times 10^2\pi$	0.8448	0.8421	0.8531	**0.6495**	0.8482
$Pe = 5 \times 10^2\pi$	0.8643	0.8619	0.8716	0.8727	**0.7153**

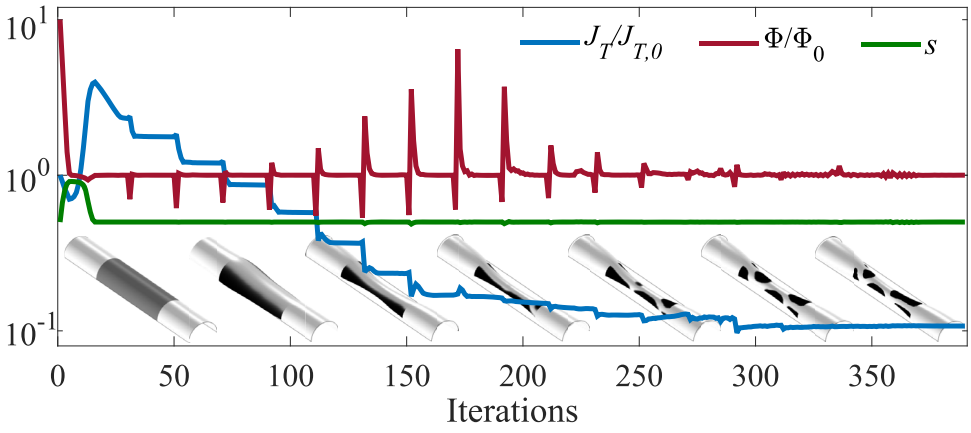

Fig. 18 Convergent histories of the design objective and constraints of the dissipation power and area fraction for heat transfer in the surface flow on the design domain sketched in Fig. 7c, including snapshots for the evolution of the fiber bundle during the iterative solution of the optimization problem

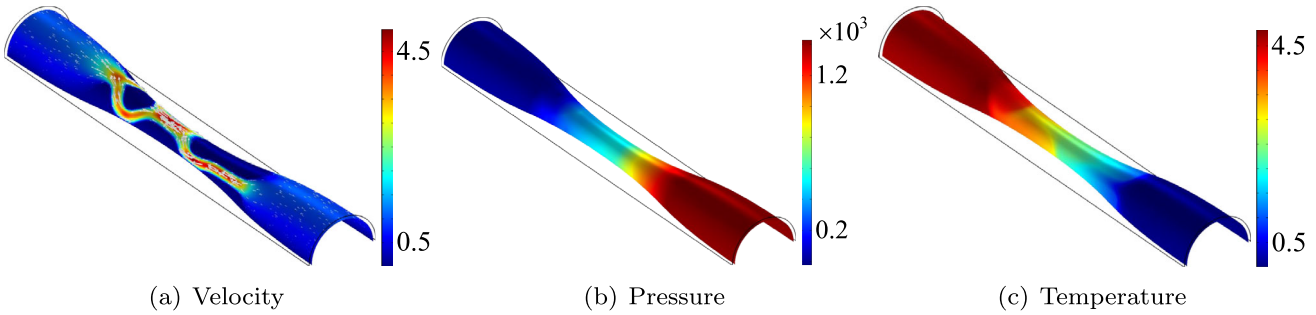

Fig. 19 Distribution of the velocity, pressure and temperature for the fiber bundle obtained on the design domain sketched in Fig. 7c

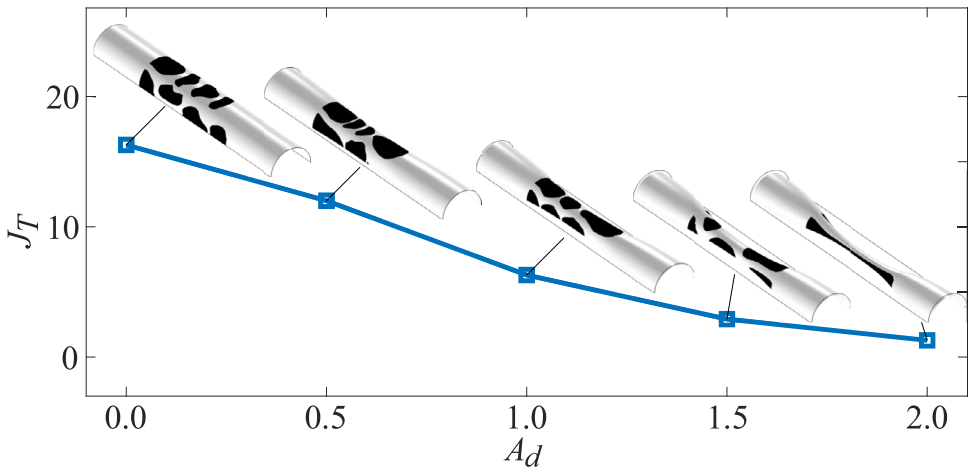

Fig. 20 Objective values for the variable magnitudes of $A_d = \{0.0, 0.5, 1.0, 1.5, 2.0\}$ and the obtained fiber bundles for heat transfer in surface flow

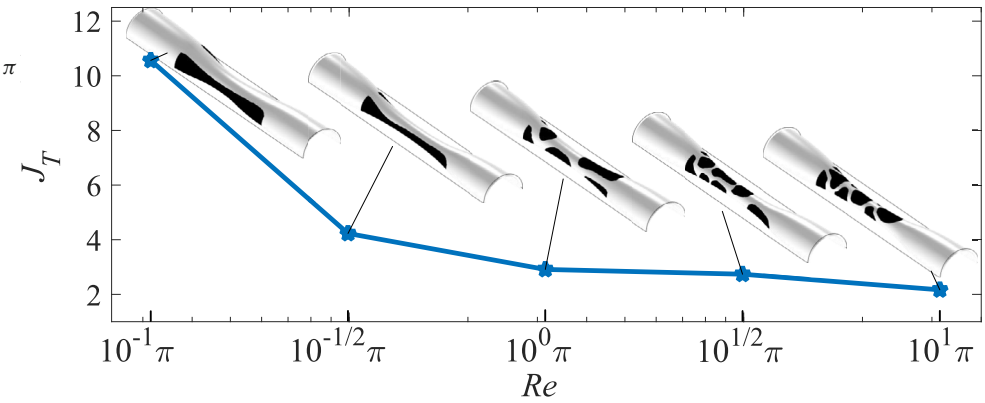

Fig. 21 Objective values for the Reynolds numbers of $Re = \{10^{-1}\pi, 10^{-1/2}\pi, 10^{0}\pi, 10^{1/2}\pi, 10^{1}\pi$ and the obtained fiber bundles for heat transfer in surface flow

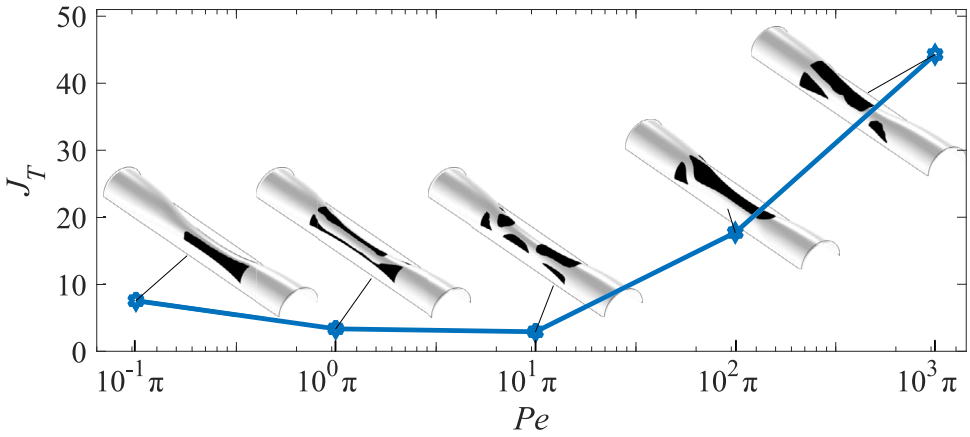

Fig. 22 Objective values for the Péclet numbers of $Pe = \{10^{-1}\pi, 10^{0}\pi, 10^{1}\pi, 10^{2}\pi, 10^{3}\pi\}$ and the obtained fiber bundles for heat transfer in surface flow

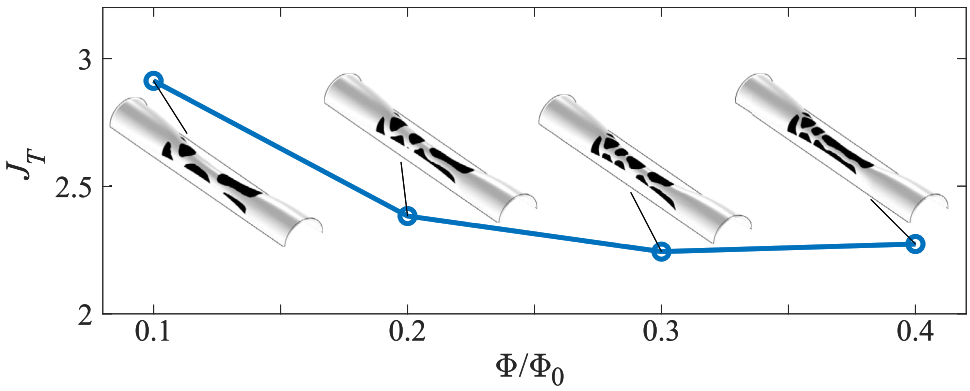

Fig. 23 Objective values for different dissipation power and the obtained fiber bundles for heat transfer in surface flow

Table 4 Objective values for the obtained fiber bundles in Fig. 22 at different Péclet numbers, where the Reynolds number is kept as $10^{0}\pi$

	 $Pe = 10^{-1}\pi$	 $Pe = 10^{0}\pi$	 $Pe = 10^{1}\pi$	 $Pe = 10^{2}\pi$	 $Pe = 10^{3}\pi$
$Pe = 10^{-1}\pi$	**7.5505**	7.7949	7.9965	8.4704	9.5489
$Pe = 10^{0}\pi$	3.7587	**3.3512**	3.9927	5.5317	6.8946
$Pe = 10^{1}\pi$	3.7922	3.5995	**2.9127**	4.9974	6.1530
$Pe = 10^{2}\pi$	25.2534	18.8232	19.3612	**17.7171**	18.3672
$Pe = 10^{3}\pi$	62.8847	51.7062	75.3778	98.3435	**44.2847**

4 Conclusions

Topology optimization on variable 2-manifolds for mass and heat transfer in surface flow has been developed to find the optimized matching between the patterns of surface structures and the implicit 2-manifolds defined with the surface patterns. It can be regarded as topology optimization on the variable design domains for mass and heat transfer in surface flow. Topology optimization for mass and heat transfer is thereby extended onto 2-manifolds with increased design freedom by incorporating the design domains into the design space. Two sets of design variables are defined for the patterns of the surface structures and the implicit 2-manifolds, where the implicit 2-manifolds are defined and evolved on the base manifolds by using differentiable homeomorphisms. Two surface-PDE filters are used to regularize the design variables. The tangential gradient operator and the unit normal vector on the implicit 2-manifolds are transformed based on the filtered design variable of the implicit 2-manifolds. Transformed forms are hence derived for the variational formulations of the surface-PDE filter of the implicit 2-manifolds and the governing equations for mass and heat transfer in surface flow. Stabilized variational formulations for the governing equations of mass and heat transfer in surface flow have been provided for the surface finite element method based numerical solutions. Continuous adjoint method has been used to analyze the topology optimization problems. In the numerical implementation, scaling factor based equivalent transformation of the constraints in the topology optimization problems is developed to scale the adjoint sensitivities of the constraints and ensure the robust satisfication of the constraints in the iterative solution procedures, by keeping the adjoint sensitivities of the constraints possess the same magnitude as that of the design objectives.

The mass and heat transfer processes in this paper are described by the surface Navier–Stokes equations, the surface convection-diffusion equation and the surface convective heat-transfer equation defined on the implicit 2-manifolds. The material distribution method is used to implement topology evolution of the surface patterns, where an artificial Darcy friction force of the porous medium is added to the surface Navier–Stokes equations. Numerical examples implemented on a series of curved surfaces obtained by deforming a flat surface into cylindrical surfaces have been presented to demonstrate the developed topology optimization approach, where the lengths of the inlet, the outlet and the wall boundaries are maintained to be unchanged during the deformation. The desired performance of the surface structures is set to achieve the anticipated distribution of the concentration at the outlets and minimize the thermal compliance in surface flow for mass and heat transfer processes, respectively. The fiber bundles are derived with the topology of the zig-zag and splitting-merging shapes for the mass and heat transfer processes, respectively.

The variable amplitude of the implicit 2-manifold, Reynolds number, Péclet number, pressure drop and dissipation power have been investigated in the numerical examples. Topology optimization problems defined on variable 2-manifolds can degenerate into the cases on fixed 2-manifolds, if the variable magnitude of the implicit 2-manifolds is set to be zero. Increasing the value of the variable amplitude can enlarge the design space of the surface structures. Convection of the surface flow can be strengthened by setting reasonable values of the Reynolds number, Péclet number, pressure drop and dissipation power to improve the desired performance of the surface structures derived in topology optimization on variable 2-manifolds. Especially, the vortex based mixing mode appears on the topologically optimized fiber bundles for mass transfer in surface flow, when the pressure drop is set to be large enough in the extended design space permitted by the variable amplitude of the implicit 2-manifolds. Experimental verifications of the topologically optimized fiber bundles for mass and heat transfer will be implemented in the future.

The developed topology optimization is limited by the variable amplitude of the implicit 2-manifolds. The variable amplitude should be set reasonably to avoid its excessive value caused problems on numerical accuracy and divergence of the related finite element solution, because the non-zero value of it gives rise to the distortion of the mapped meshes on the implicit 2-manifolds. This limitation can be solved by using the homotopy theory to relax the rigidity of the bijections defined by the normal displacement on the base manifolds and adaptive meshes in the finite element solution. Laminar flow is considered for the surface flow in this paper and this research can be extended to the turbulent flow.

Supplementary Information The online version contains supplementary material available at https://doi.org/10.1007/s00158-025-04216-3.

Acknowledgements The authors acknowledge support by the state of Baden-Württemberg through bwHPC in Germany. They are grateful to Prof. K. Svanberg of KTH for supplying the codes for the method of moving asymptotes.

Author Contributions Both authors contributed to the formulation of the numerical technique herein presented. Yongbo Deng conducted all mathematical derivations, wrote the computer code, performed the numerical experiments, drew initial conclusions, and drafted the paper. Both authors edited the final version of the manuscript.

Funding Open Access funding enabled and organized by Projekt DEAL. YD and JGK acknowledge support from the DFG under grant KO 1883/20-1 Metacoils and the German Excellence Initiative under grant EXC 2082 "3D Matter Made to Order"; JGK acknowledges support from the ERC-SyG (HiSCORE, 951459) and partial support from CRC 1527 HyPERiON.

Data Availability Source code and data used for these results will be made available upon request.

Declarations

Conflict of interest The authors states that there is no Conflict of interest.

References

Aage N, Poulsen TH, Gersborg-Hansen A, Sigmund O (2008) Topology optimization of large scale stokes flow problems. Struct Multidisc Optim 35:175–180

Akl W, El-Sabbagh A, Al-Mitani K, Baz A (2008) Topology optimization of a plate coupled with acoustic cavity. Int J Solids Struct 46:2060–2074

Alexandersen J, Aage N, Andreasen CS, Sigmund O (2013) Topology optimisation for natural convection problems. Int J Numer Meth Fluids 00:1–23

Allaire G (2002) Shape optimization by the homogenization method. Springer-Verlag, New York

Allaire G, Jouve F, Toader A (2004) Structural optimization using sensitivity analysis and a level-set method. J Comput Phys 194:363–393

Andreasen CS (2012) A topology optimization interface for LS-DYNA. In: Aulig N, Lepenies I (eds), 11. LS-DYNA Forum, Ulm

Andreasen CS (2019) A framework for topology optimization of inertial microfluidic particle manipulators. Struct Multidisc Optim 61:2418–2499

Andreasen CS, Gersborg AR, Sigmund O (2009) Topology optimization of microfluidic mixers. Int J Numer Meth Fluids 61:498–513

Ansola R, Canales J, Tárrago JA, Rasmussen J (2002) An integrated approach for shape and topology optimization of shell structures. Comput Struct 80:449–458

Arroyo M, DeSimone A (2009) Relaxation dynamics of fluid membranes. Phys Rev E 79:031915

Behrou R, Lawry M, Maute K (2017) Level set topology optimization of structural problems with interface cohesion. Int J Numer Meth Eng 112:990–1016

Bendsøe MP, Kikuchi N (1988) Generating optimal topologies in optimal design using a homogenization method. Comput Methods Appl Mech Eng 71:197–224

Bendsøe MP, Sigmund O (2003) Topology optimization-theory methods and applications. Springer, Berlin

Bendsøye MP, Sigmund O (1999) Material interpolations in topology optimization. Arch Appl Mech 69:635–654

Bhattacharjee D, Atta A (2022) Topology optimization of a packed bed microreactor involving pressure driven non-Newtonian fluids. React Chem Eng 7:609

Borrvall T, Petersson J (2003) Topology optimization of fluid in Stokes flow. Int J Numer Meth Fluids 41:77–107

Brenner H (2013) Interfacial transport processes and rheology. Phys. Rev. E, Elsevier

Challis VJ, Guest JK (2009) Level set topology optimization of fluids in Stokes flow. Int J Numer Meth Eng 79:1284–1308

Chen Y, Chen X, Liu S (2021) Numerical investigations on influence factors in topology optimization for catalytic microreactors. J Dispersion Sci Technol 42:1431–1438

Cheng KT, Olhoff N (1981) An investigation concerning optimal design of solid elastic plates. Int J Solids Struct 17:305–323

Chern SS, Chen WH, Lam KS (1999) Lectures on differential geometry. World Scientific

Clausen A, Andreassen E, Sigmund O (2017) Topology optimization of 3D shell structures with porous infill. Acta Mech Sinica 33:778–791

Deng Y, Liu Z, Zhang P, Liu Y, Wu Y (2011) Topology optimization of unsteady incompressible Navier-Stokes flows. J Comput Phys 230:6688–6708

Deng Y, Liu Z, Zhang P, Liu Y, Wu Y, Gao Q, Wu Y (2012) A flexible layout design method for passive micromixers. Biomed Microdevices 14:929–945

Deng Y, Liu Z, Wu Y (2013a) Topology optimization of steady and unsteady incompressible Navier-Stokes flows driven by body forces. Struct Multidisc Optim 47:555–570

Deng Y, Liu Z, Wu J, Wu Y (2013b) Topology optimization of steady Navier-Stokes flow with body force. Comput Methods Appl Mech Eng 255:306–321

Deng Y, Zhou T, Liu Z, Wu Y, Qian S, Korvink JG (2018) Topology optimization of electrode patterns for electroosmotic micromixer. Int J Heat Mass Transfer 126:1299–1315

Deng Y, Mager D, Bai Y, Zhou T, Liu Z, Wen L, Wu Y, Korvink JG (2018) Inversely designed micro-textures for robust Cassie-Baxter mode of super-hydrophobicity. Comput Methods Appl Mech Eng 341:113–132

Deng Y, Liu Z, Wang Y, Duan H, Korvink JG (2019) Micro-textures inversely designed with overlayed-lithography manufacturability for wetting behavior in Cassie-Baxter status. Appl Math Model 74:621–640

Deng Y, Zhang W, Liu Z, Zhu J, Korvink JG (2020) Fiber bundle topology optimization of hierarchical microtextures for wetting behavior in Cassie-Baxter mode. Struct Multidisc Optim 61:2523–2556

Deng Y, Liu Z, Korvink JG (2020) Topology optimization on two-dimensional manifolds. Comput Methods Appl Mech Eng 364:112937

Deng Y, Zhang W, Liu Z, Zhu J, Korvink JG (2022) Topology optimization for surface flows. J Comput Phys 467:111415

Deng Y, Zhang W, Liu Z, Zhu J, Xu Y, Korvink JG (2024) Fiber bundle topology optimization for surface flows. Chi J Mech Eng 37:55

Deng Y, Liu Z, Zhang P, Wu Y, Korvink JG (2010) Optimization of no-moving part fluidic resistance microvalves with low Reynolds number. IEEE international conference on optical MEMS 8 April, Hongkong

Deng Y, Liu Z, Zhang P, Wu Y, Korvink JG (2010) Optimization of no-moving-part fluidic resistance microvalves with low Reynolds number. IEEE MEMS conference, pp 67–70

Deng Y, Wu Y, Xuan M, Korvink JG, Liu Z (2011) Dynamic optimization of valveless micropump. In: International conference on solid state sensors and actuators (TRANSDUCERS) 5-9 June, Beijing

Dienemann R, Schumacher A, Fiebig S (2017) Topology optimization for finding shell structures manufactured by deep drawing. Struct Multidisc Optim 56:473–485

Dilgen CB, Dilgen SB, Fuhrman DR, Sigmund O, Lazarov BS (2018) Topology optimization of turbulent flows. Comput Methods Appl Mech Eng 331:363–393

Duhring MB, Jensen JS, Sigmund O (2008) Acoustic design by topology optimization. J Sound Vib 317:557–575
Dziuk G, Elliott CM (2013) Finite element methods for surface PDEs. Acta Numer 22:289–396
Fawaz A, Hua Y, Corre SL, Fan Y, Luo L (2022) Topology optimization of heat exchangers: a review. Energy 252:124053
Fries TP (2018) Higher-order surface FEM for incompressible Navier-Stokes flows on manifolds. Int J Numer Meth Fl 88:55–78
Gao T, Zhang W (2011) A mass constraint formulation for structural topology optimization with multiphase materials. Int J Numer Meth Eng 88:774–796
Gersborg-Hansen A, Sigmund O, Haber RB (2005) Topology optimization of channel flow problems. Struct Multidisc Optim 29:1–12
Gersborg-Hansen A, Bendsøe MP, Sigmund O (2006) Topology optimization of heat conduction problems using the finite volume method. Struct Multidisc Optim 31:251–259
Gersborg-Hansen A, Bendsøe MP, Sigmund O (2006) Topology optimization of heat conduction problems using the finite volume method. Struct Multidisc Optim 31:251–259
Guest JK, Proevost JH (2006) Topology optimization of creeping fluid flows using a Darcy-Stokes finite element. Int J Numer Meth Eng 66:461–484
Guest J, Prévost J, Belytschko T (2004) Achieving minimum length scale in topology optimization using nodal design variables and projection functions. Int J Numer Methods Eng 61:238–254
Guillaume PH, Idris KS (2004) Topological sensitivity and shape optimization for the Stokes equations. SIAM J Cont Optim 43:1–31
Guo X, Zhang W, Zhong W (2014) Doing topology optimization explicitly and geometrically—a new moving morphable components based framework. J Appl Mech 81:081009
Guo X, Zhang W, Zhang J, Yuan J (2016) Explicit structural topology optimization based on moving morphable components (MMC) with curved skeletons. Comput Methods Appl Mech Eng 310:711–748
Hammond J, Pietropaoli M, Montomoli F (2022) Topology optimisation of turbulent flow using data-driven modelling. Struct Multidisc Optim 65:49
Hassani B, Tavakkoli SM, Ghasemnejad H (2013) Simultaneous shape and topology optimization of shell structures. Struct Multidisc Optim 48:221–233
Hinze M, Pinnau R, Ulbrich M, Ulbrich S (2009) Optimization with PDE constraints. Phys. Fluids, Springer, Berlin
Høghøj LC (2023) Topology Optimization of strucures with heat and mass transfer. Technical University of Denmark. DCAMM Special Report No. S336
Høghøj LC, Nørhavea DR, Alexandersen J, Sigmund O, Andreasen CS (2020) Topology optimization of two fluid heat exchangers. Int J Heat Mass Transf 163:120543
https://www.comsol.com
https://www.mathworks.com
Huang X, Xie YM (2010) A further review of ESO type methods for topology optimization. Struct Multidiscip Optim 41:671–683
Huo W, Liu C, Du Z, Jiang X, Liu Z, Guo X (2022) Topology optimization on complex surfaces based on the moving morphable component method and computational conformal mapping. J Appl Mech 89:051008
Joo Y, Lee I, Kim SJ (2017) Topology optimization of heat sinks in natural convection considering the effect of shape-dependent heat transfer coefficient. Int J Heat Mass Transf 109:123–133
Kown Y, Patankar N, Choi J, Lee J (2009) Design of surface hierarchy for extreme hydrophobicity. Langmuir 25:6129–6136
Kreissl S, Pingen G, Maute K (2011) An explicit level-set approach for generalized shape optimization of fluids with the lattice Boltzmann method. Int J Numer Meth Fluids 65:496–519
Krog L, Olhoff N (1996) Optimum topology and reinforcement design of disk and plate structures with multiple Stiffness and Eigen frequency objectives. Comput Methods Appl Mech Eng 72:535–563
Li B, Hong J, Liu G, Ge L (2018) On identifying optimal heat conduction topologies from heat transfer paths analysis. Int Commun Heat Mass Transf 90:93–102
Li H, Ding X, Meng F, Jing D, Xiong M (2019) Optimal design and thermal modelling for liquid-cooled heat sink based on multi-objective topology optimization: an experimental and numerical study. Int J Heat Mass Transf 144:118638
Liu Z, Korvink JG (2008) Adaptive moving mesh level set method for structure optimization. Eng Optim 40:529–558
Liu Z, Deng Y, Lin S, Xuan M (2012) Optimization of micro Venturi diode in steady flow at low Reynolds number. Eng Optim 44:1389–1404
Lochner-Aldinger I, Schumacher A (2014) Homogenization method. In: Adriaenssens S, Block P, Veenendaal D, Williams C (eds) Shell structures for architecture-form finding and optimization. J Sound Vib. Routledge, New York
Lohan DJ, Dede EM, Allison JT (2017) Topology optimization for heat conduction using generative design algorithms. Struct Multidisc Optim 55:1063–1077
Lundgaard C, Alexandersen J, Zhou M, Andreasen CS, Sigmund O (2018) Revisiting density-based topology optimization for fluid-structure-interaction problems. Struct Multidisc Optim 82:969–995
Luo YJ, Kang Z, Yue ZF (2012) Maximal stiffness design of two-material structures by topology optimization with nonprobabilistic reliability. AIAA J 50:1993–2003
Marck G, Nemer M, Harion JL (2013) Topology optimization of heat and mass transfer problems: laminar flow. Numer Heat Transfer Part B Fund 63:508–539
Michell AGM (1904) The limit of economy of material in frame-structures. Phil Mag 8:589–597
Miralles V, Huerre A, Malloggi F, Jullien MC (2013) A review of heating and temperature control in microfluidic systems: techniques and applications. Diagnostics 3:33–67
Nabaki K, Shen J, Huang X (2018) Stress minimization of structures based on bidirectional evolutionary procedure. J Struct Eng 145:04018256
Nguyen NT, Wu Z (2005) Micromixers—a review. J Micromech Microeng 15:R1
Nomura T, Sato K, Taguchi K, Kashiwa T, Nishiwaki S (2007) Structural topology optimization for the design of broadband dielectric resonator antennas using the finite difference time domain technique. Int J Numer Meth Eng 71:1261–1296
Okkels F, Bruus H (2006) Design of micro-fluidic bio-reactors using topology optimization. European Conference on Computational Fluid Dynamics TU Delft, The Netherlands
Olessen LH, Okkels F, Bruus H (2006) A high-level programming-language implementation of topology optimization applied to steady-state Navier-Stokes flow. Int J Numer Meth Eng 65:975–1001
Pietropaoli M, Montomoli F, Gaymann A (2019) Three-dimensional fluid topology optimization for heat transfer. Struct Multidisc Optim 59:801–812
Pingen G, Maute K (2010) Optimal design for non-Newtonian flows using a topology optimization approach. Comput Math Appl 59:2340–2350
Rahimi M, DeSimone A, Arroyo M (2013) Curved fluid membranes behave laterally as effective viscoelastic media. Soft Matter 9:11033–11045
Raulli M, Maute K (2005) Topology optimization of electrostatically actuated microsystems. Struct Multidisc Optim 30:342–359
Reuther S, Voigt A (2018) Solving the incompressible surface Navier-Stokes equation by surface finite elements. Phys Fluids 30:012107

Rogié B, Andreasen CS (2023) Design complexity tradeoffs in topology optimization of forced convection laminar flow heat sinks. Struct Multidisc Optim 66:6

Rozvany GIN (2001) Aims, scope, methods, history and unified terminology of computer-aided topology optimization in structural mechanics. Struct Multidisc Optim 21:90–108

Sá LFN, Yamabe PVM, Souza BC, Silva ECN (2021) Topology optimization of turbulent rotating flows using Spalart–Allmaras model. Comput Methods Appl Mech Eng 373:113551

Saxena A (2005) Topology design of large displacement compliant mechanisms with multiple materials and multiple output ports. Struct Multidisc Optim 30:477–490

Schäpper D, Fernandes RL, Lantz AE, Okkels F, Bruus H, Gernaey KV (2011) Topology optimized microbioreactors. Biotech Bioeng 108:786–796

Sigmund O (1997) On the design of compliant mechanisms using topology optimization. Mech Struct Mach 25:495–526

Sigmund O (2001) A 99-line topology optimization code written in Matlab. Struct Multidisc Optim 21:120–127

Sigmund O, Hougaard KG (2008) Geometric properties of optimal photonic crystals. Phys Rev Lett 100:153904

Sigmund O, Torquato S (1997) Design of materials with extreme thermal expansion using a three-phase. Mech Phys Solid 45:1037–1067

Sritharan SS (1998) Optimal control of viscous flow. SIAM, Philadelphia

Steven GP, Li Q, Xie YM (2000) Evolutionary topology and shape design for physical field problems. Comput Meth Appl Mech Eng Comput Mech 26:129–139

Svanberg K (1987) The method of moving asymptotes: a new method for structural optimization. Int J Numer Meth Eng 24:359–373

Takezawa A, Nishiwaki S, Kitamura M (2010) Shape and topology optimization based on the phase field method and sensitivity analysis. J Comput Phys 229:2697–2718

Tawk R, Ghannam B, Nemer M (2019) Topology optimization of heat and mass transfer problems in two fluids—one solid domains. Numer Heat Trans Part B Fund 76:130–151

Thimbleby H (1989) The Leidenfrost phenomenon. Phys Educ 24:300–303

Vermaak N, Michailidis G, Parry G, Estevez R, Allaire G, Bréchet Y (2014) Material interface effects on the topology optimization of multi-phase structures using a level set method. Struct Multidisc Optim 50:623–644

Vogiatzis P, Ma M, Chen S, Gu X (2018) Computational design and additive manufacturing of periodic conformal metasurfaces by synthesizing topology optimization with conformal mapping. Comput Methods Appl Mech Eng 328:477–497

Wang MY, Wang XM (2004) "Color" level sets: a multi-phase method for structural topology optimization with multiple materials. Comput Methods Appl Mech Eng 193:469–496

Wang MY, Wang X, Guo D (2003) A level set method for structural optimization. Comput Meth Appl Mech Eng 192:227–246

Wang F, Lazarov BS, Sigmund O (2011) On projection methods, convergence and robust formulations in topology optimization. Struct Multidiscip Optim 43:767–784

Wang J, Liu X, Wang Y (2023) Topology optimization of micro-channel reactors using an improved multi-objective algorithm. Chem Eng J 458:141420

Wiker N, Klarbring A, Borrvall T (2007) Topology optimization of regions of Darcy and Stokes flow. Int J Numer Meth Eng 69:1374–1404

Xia Q, Wang MY (2008) Topology optimization of thermoelastic structures using level set method. Comput Mech 42:837–857

Xia Y, Chen L, Luo J, Tao W (2023) Numerical investigation of microchannel heat sinks with different inlets and outlets based on topology optimization. Appl Energy 330:120335

Xing X, Wei P, Wang MY (2010) A finite element-based level set method for structural optimization. Int J Numer Meth Eng 82:805–842

Xue S, Ma X, Liu D, Huo ZK, Hao P, Wang B (2024) Thermoelastic topology optimization for stiffened thin-walled structures under design-dependent thermal loading problems. Comput Meth Appl Mech Eng 42:117344

Yan K, Cheng GD, Wang BP (2018) Topology optimization of damping layers in shell structures subject to impact loads for minimum residual vibration. J Sound Vib 431:226–247

Yan K, Wang YY, Pan Y, Sun G, Chen J, Cai XH, Cheng GD (2023) Topology optimization of simplified convective heat transfer problems using the finite volume method. Sci China Technol Sci 66:1352–1364

Yao X, Zhang Y, Du L, Liu J, Yao J (2015) Review of the applications of microreactors. Renew Sustain Energy Rev 47:519–539

Yoon GH (2010) Topology optimization for stationary fluid-structure interaction problems using a new monolithic formulation. Int J Numer Meth Eng 82:591–616

Yoon GH (2016) Topology optimization for turbulent flow with Spalart–Allmaras model. Comput Methods Appl Mech Eng 303:288–311

Zhang W, Feng S (2022) Combined parameterization of material distribution and surface mesh for stiffener layout optimization of complex surfaces. Struct Multidisc Optim 65:103

Zhang B, Gao L (2019) Topology optimization of convective heat transfer problems for non-Newtonian fluids. Struct Multidisc Optim 60:1821–1840

Zhang Y, Liu S (2008) Design of conducting paths based on topology optimization. Heat Mass Transfer 44:1217–1227

Zhou S, Li Q (2008) A variational level set method for the topology optimization of steady-state Navier-Stokes flow. J Comput Phys 227:10178–10195

Zhou SW, Wang MY (2007) Multimaterial structural topology optimization with a generalized Cahn-Hilliard model of multiphase transition. Struct Multidisc Optim 33:89–111

Zhou Y, Zhang W, Zhu J, Xu Z (2016) Feature-driven topology optimization method with signed distance function. Comput Methods Appl Mech Eng 310:1–32